Title
Defining functional classes of Barth syndrome mutation in humans

Journal
Human Molecular Genetics, 25(9)

ISSN
0964-6906

Authors
Lu, Ya-Wen
Galbraith, Laura
Herndon, Jenny D
et al.

Publication Date
2016-05-01

DOI
10.1093/hmg/ddw046

Peer reviewed

OXFORD

Human Molecular Genetics, 2016, Vol. 25, No. 9 1754–1770

doi: 10.1093/hmg/ddw046
Advance Access Publication Date: 16 February 2016
Original Article

ORIGINAL ARTICLE

Defining functional classes of Barth syndrome mutation in humans

Ya-Wen Lu[1], Laura Galbraith[2], Jenny D. Herndon[3], Ya-Lin Lu[4], Mia Pras-Raves[5], Martin Vervaart[5], Antoine Van Kampen[6], Angela Luyf[6], Carla M. Koehler[3], J.Michael McCaffery[7], Eyal Gottlieb[2], Frederic M. Vaz[5] and Steven M. Claypool[1,*]

[1]Department of Physiology, Johns Hopkins University School of Medicine, Baltimore, MD 21205-2185, USA, [2]Cancer Research UK, The Beatson Institute for Cancer Research, Glasgow G61 1BD, UK, [3]Department of Chemistry and Biochemistry, Molecular Biology Institute, and Jonsson Comprehensive Cancer Center, University of California, Los Angeles, CA 90095-1569, USA, [4]Division of Biology and Biomedical Sciences, Graduate School of Arts and Sciences, Washington University, St. Louis, MO 63130-4899, USA, [5]Departments of Clinical Chemistry and Pediatrics, Laboratory Genetic Metabolic Diseases and [6]Bioinformatics Laboratory, Department of Clinical Epidemiology, Biostatistics and Bioinformatics, Academic Medical Center, Amsterdam, The Netherlands and [7]Integrated Imaging Center, Department of Biology, Johns Hopkins University, Baltimore, MD 21218, USA

*To whom correspondence should be addressed at: Department of Physiology, Johns Hopkins School of Medicine, 725 N. Wolfe Street, Baltimore, MD 21205-2185, USA. Tel: +1 410 614 1786; Fax: +1 410 955 0461; Email: sclaypo1@jhmi.edu

Abstract

The X-linked disease Barth syndrome (BTHS) is caused by mutations in *TAZ*; TAZ is the main determinant of the final acyl chain composition of the mitochondrial-specific phospholipid, cardiolipin. To date, a detailed characterization of endogenous TAZ has only been performed in yeast. Further, why a given BTHS-associated missense mutation impairs TAZ function has only been determined in a yeast model of this human disease. Presently, the detailed characterization of yeast tafazzin harboring individual BTHS mutations at evolutionarily conserved residues has identified seven distinct loss-of-function mechanisms caused by patient-associated missense alleles. However, whether the biochemical consequences associated with individual mutations also occur in the context of human TAZ in a validated mammalian model has not been demonstrated. Here, utilizing newly established monoclonal antibodies capable of detecting endogenous TAZ, we demonstrate that mammalian TAZ, like its yeast counterpart, is localized to the mitochondrion where it adopts an extremely protease-resistant fold, associates non-integrally with intermembrane space-facing membranes and assembles in a range of complexes. Even though multiple isoforms are expressed at the mRNA level, only a single polypeptide that co-migrates with the human isoform lacking exon 5 is expressed in human skin fibroblasts, HEK293 cells, and murine heart and liver mitochondria. Finally, using a new genome-edited mammalian BTHS cell culture model, we demonstrate that the loss-of-function mechanisms for two BTHS alleles that represent two of the seven functional classes of BTHS mutation as originally defined in yeast, are the same when modeled in human TAZ.

Introduction

The boundaries of cells and organelles are marked by membranes that differ in their phospholipid and protein compositions. The collection of phospholipids, including their associated fatty acyl chains, that establish a defined membrane-bound compartment confer unique membrane properties (curvature and rigidity) and contribute to numerous functions that occur at/across the

Received: January 12, 2016. **Revised:** February 8, 2016. **Accepted:** February 15, 2016

membrane surface (transport and signaling) or within the space that it confines. As such, changes in membrane lipid composition can directly impact numerous fundamental cellular processes. A particularly salient example of the importance of proper lipid composition for organelle function is provided by the mitochondrion, the powerhouse of the cell, and its signature phospholipid, cardiolipin (CL).

CL is required for a diversity of basic processes that are central to mitochondrial biology (1). In fact, CL is of such fundamental importance that mammalian development fails *in utero* in its absence (2). CL is a dimer of two phosphatidic acids linked together by a glycerol bridge. CL associates with numerous mitochondrial proteins, including every oxidative phosphorylation (OXPHOS) complex/component, many solute carriers, and translocases in both the outer and inner mitochondrial membranes (IMMs) (3–5). Collectively, these interactions with CL stabilize individual proteins and multisubunit complexes, and can stimulate enzyme activity either directly (e.g. serve a catalytic function (6)) or secondarily (e.g. promote the assembly of individual respiratory complexes into more efficient supercomplexes (7–9)). Finally, CL serves as a signal that is detected by CL-binding proteins with downstream consequences that range from mitochondrial fission and IMM fusion (10,11) to apoptosis and mitophagy (12,13).

The biosynthesis of CL occurs through a reaction series that is highly conserved from yeast to humans (14). With respect to its acyl chain composition, the CL that is newly produced is not what accumulates at steady state, which is highly homogeneous and characterized by increased acyl chain unsaturation and molecular symmetry (15). The steady-state form of CL is established by an acyl chain remodeling process that begins with the removal of a fatty acyl chain from CL by a deacylase(s), generating monolysocardiolipin (MLCL), which is then re-acylated by the evolutionarily conserved MLCL transacylase, tafazzin (TAZ) (16). Mutations in *TAZ* result in the X-linked cardio- and skeletal myopathy, Barth syndrome (BTHS) (17,18). In the absence of TAZ, there is less CL, the remodeling precursor and product, and more MLCL, the remodeling intermediate (19). Further, the CL that remains has an abnormal acyl chain profile (15,20). These BTHS-associated changes in mitochondrial phospholipid composition destabilize respiratory supercomplexes, reduce OXPHOS efficiency, increase reactive oxygen species production and impair sarcomere organization (21–24).

BTHS is the founding member of a new class of mitochondrial disorder that results from nuclear defects that impact mitochondrial phospholipid metabolism (25). Notably, some of the disorders, including dilated cardiomyopathy with ataxia (DCMA), Sengers and MEGDEL syndromes, in this new class of mitochondrial disease share some biochemical phenotypes with BTHS. In each case, changes in the acyl chain pattern, abundance and/or submitochondrial distribution of CL are postulated to contribute to disease pathogenesis (26–29). However, their exact pathogenic mechanisms have not been established and thus the basis for the shared and unique phenotypes of this cohort of syndromes is presently unclear.

Currently, a detailed topological map of TAZ-based CL remodeling has only been drawn in the yeast *Saccharomyces cerevisiae*. In yeast, all of the steps up to and including the initiation of the remodeling process occur on the matrix side of the IMM (14). In contrast, yeast Taz1 is anchored to both the IMM and outer mitochondrial membrane (OMM) facing the intermembrane space (IMS) by virtue of a membrane anchor that protrudes into but not completely through the lipid bilayer (30). Thus, in yeast, CL remodeling involves an obligate trafficking step of MLCL from one side of the IMM to the other. Further, a yeast BTHS model has been exploited to determine the disease pathogenicity of a multitude of patient-associated missense alleles. To date, seven distinct pathogenic loss-of-function (LOF) mechanisms have been identified (30–32). Thus at present, our understanding of the basic cell biology of this clinically important remodeling pathway and the biochemical abnormalities associated with any genetic lesion linked to BTHS is based solely on work in yeast.

Here, we show that mammalian TAZ is localized to the mitochondrion where it adopts an extremely protease-resistant fold, associates non-integrally with IMS-facing membranes and assembles in a range of complexes. Even though multiple isoforms are expressed at the transcript level, only a single TAZ polypeptide that co-migrates with the human isoform lacking exon 5 is detected in mitochondria isolated from human skin fibroblasts, HEK293 cells, and murine heart and liver. Utilizing a newly established mammalian BTHS cell model, we determined that the two pathogenic mutations tested result in the same biochemical consequences when modeled in human TAZ as originally defined in yeast. Interestingly, overexpression of the unstable R57L mutant which lacks transacylase activity *in vitro*, partially rescues the mitochondrial CL and MLCL abnormalities of the *taz*-deficient cells *in vivo*, suggesting that strategies aimed at stabilizing this mutant allele could be of therapeutic benefit.

Results

Mammalian TAZ is localized to the mitochondrion

The absence of antibodies capable of detecting endogenous TAZ has significantly impeded progress in our understanding of BTHS pathogenesis. To overcome this obstacle, three TAZ-specific mouse monoclonal antibodies (mAb; 2G3F7, 3D7F11 and 2C2C9) were generated. Critically, each mAb detected endogenous TAZ in fibroblast cell extracts from healthy controls (C109) but not two BTHS patients (TAZ001 and TAZ003) (Fig. 1A). TAZ001 encodes a truncated 50 amino acid protein while TAZ003 has a single R57L missense allele in TAZ (20). Using these new reagents, endogenous TAZ co-fractionated with mitochondria (Fig. 1B) and was detected in both human and murine mitochondria (Fig. 1C).

Human TAZ mRNA is present as a number of splice variants (20,33). To determine the capacity of the three mAbs to detect different TAZ isoforms, the epitope recognized by each mAb was mapped; each of the three mAbs binds an epitope that is present in a different exon (Fig. 1D). Moreover, they each have the capacity to recognize every predicted isoform based on mRNA analyses (20,33). Following immunoprecipitation of TAZ with one mAb (3D7F11), only a single TAZ band was detected by immunoblot using a second mAb (2C2C9) in control but not BTHS cell extracts (Fig. 1E). Finally, based on co-migration with assorted human TAZ isoforms expressed in *taz1Δ* yeast (34), all of the cells and tissues surveyed only express TAZ lacking exon 5 (TAZ-ex5; exon 5 is missing in rodents so full-length murine TAZ already lacks exon 5) (Fig. 1F). Thus, TAZ-ex5 is likely the major isoform expressed at the protein-level *in vivo*.

Generation of a mammalian BTHS cell model

To establish a new mammalian BTHS cell culture model, we utilized TALEN-mediated genome editing in 293 Flp-In cells to introduce genetic lesions within *TAZ* exon 1. Two taz^{TALEN} clones were identified that had undetectable levels of TAZ protein (Fig. 2B) and which contained genomic deletions in the targeted locus (Fig. 2A). In both taz^{TALEN}.2 and 19, a proline that is highly

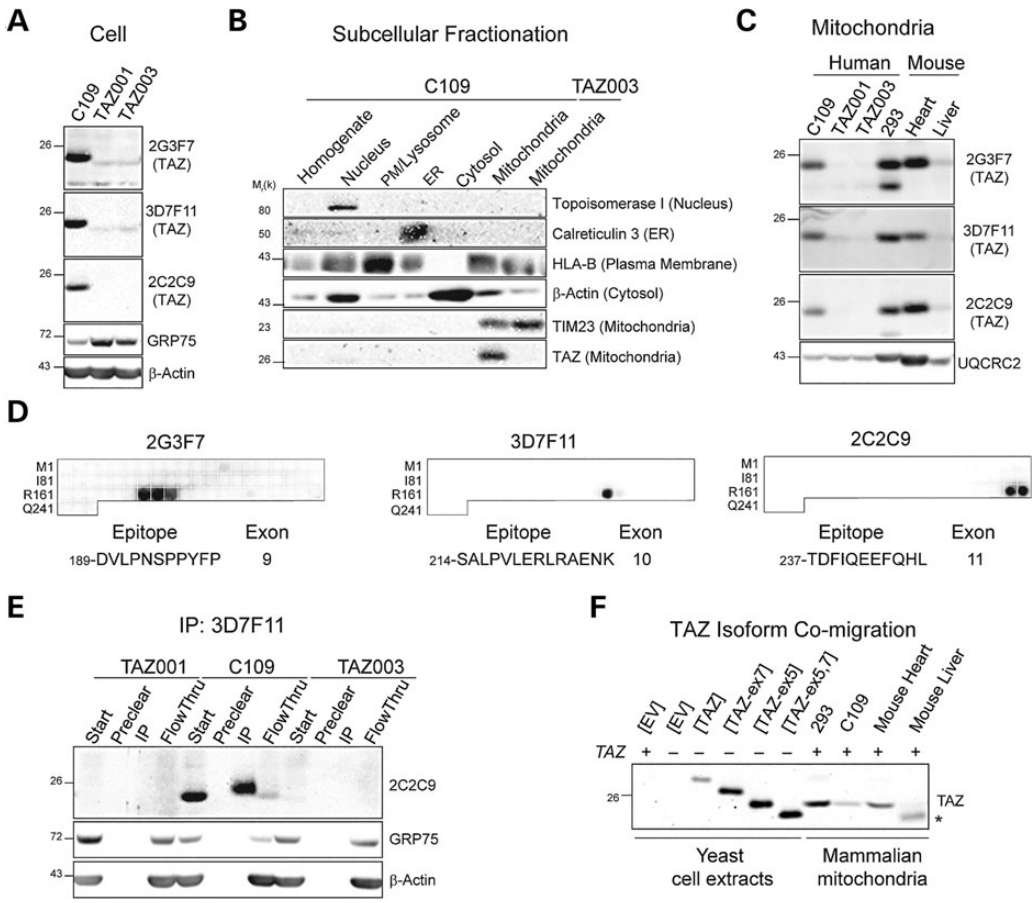

Figure 1. One isoform of TAZ is expressed and localized to mitochondria in mammalian cells and tissues. (**A**) Whole cell extracts (50 μg) from healthy control (C109) and BTHS patient fibroblasts (TAZ001 and TAZ003) were immunoblotted with three different mAbs generated against recombinant human TAZ. (**B**) Subcellular fractions (50 μg) derived from C109 cells immunoblotted as indicated. (**C**) Mitochondrial extracts (50 μg) from the indicated source immunoblotted with the TAZ mAbs. (**D**) The epitope recognized by each TAZ mAb was determined by peptide array. The exon that harbors each epitope is indicated. (**E**) TAZ was immunoprecipitated with 3D7F11 from 1.5 mg of the indicated cell extracts. Fifty micrograms of starting material and non-binding flow through and 100% of bound material (Preclear and IP) were immunoblotted using 2C2C9. (**F**) Whole cell extracts from WT or *taz1*Δ yeast transformed as indicated and mitochondrial extracts from the designated source immunoblotted for TAZ. EV, empty vector. *nonspecific band.

conserved in mammals but not in fungi, is deleted (Supplementary Material, Fig. S1); in addition, there was a missense mutation (V12A) identified in *taz*^{TALEN}.19 and five additional amino acids removed (amino acids 11–16) in *taz*^{TALEN}.2. Surprisingly, neither deletion altered the overall reading frame of TAZ. Based on *in silico* analyses (Supplementary Material, Table S1), we hypothesize that Pro13 is either a critical determinant of a non-bilayer spanning membrane anchor and/or essential for TAZ folding and stability. Consistent with these possibilities, proteosomal inhibition with MG132 did not stabilize TAZ in either *taz*^{TALEN} cell line (Fig. 2C). The lack of protein expression did not reflect differences in TAZ mRNA levels (Fig. 2D). Moreover, the expression of representative proteins of each mitochondrial subcompartment and every OXPHOS complex was the same in mitochondria isolated from each *taz*^{TALEN} cell line as WT (Fig. 2E and F). Of note, the expression of PHB2 and DNAJC19, proteins functionally linked to TAZ (28), was also not altered in either *taz*^{TALEN} cell line. Finally, as matrix-targeted Su9-DHFR was imported into mitochondria isolated from both *taz*^{TALEN} cells at rates similar to that of WT mitochondria, the membrane potential across the IMM is not grossly impaired in the *taz*^{TALEN} cells (Fig. 2G and H).

Next, the phospholipid composition of mitochondria isolated from WT and *taz*^{TALEN} cells was determined by mass spectrometry. An increased MLCL:CL ratio is a biochemical hallmark of TAZ deficiency (36). Importantly, mitochondria from each *taz*^{TALEN} cell contained a significantly increased MLCL:CL ratio (Fig. 3C) that was largely driven by an accumulation of MLCL (Fig. 3B). The amount of CL was not significantly changed (Fig. 3A). TAZ-based CL remodeling is a major determinant of the final acyl chain composition of CL at the steady state, which is typified by the inclusion of more unsaturated acyl chains compared with pre-remodeled CL. While there were only modest changes in CL acyl chain length in the *taz*^{TALEN} cells (Fig. 3E), the amount of CL containing fewer double bonds was significantly increased (Fig. 3F). Moreover, the relative abundance of unsaturated acyl chains for CL molecules of a given length was consistently lower in *taz*^{TALEN} than in WT mitochondria (Fig. 3G–K). In addition to its dramatically increased abundance, there were also notable changes in the acyl chain profile of the remodeling intermediate MLCL in mitochondria isolated from both *taz*^{TALEN} cells (Fig. 3L–O). Specifically, MLCL with longer acyl chains that contained fewer double bonds accumulated in the absence of TAZ activity. Other alterations in the mitochondrial lipidome that were consistent features of mitochondria from both *taz*^{TALEN} cells included an increased abundance of phosphatidylglycerol (PG; Fig. 3D), bis-monoacylglyerol phosphate, reduced levels of phosphatidylinositol and subtle changes in the acyl chain

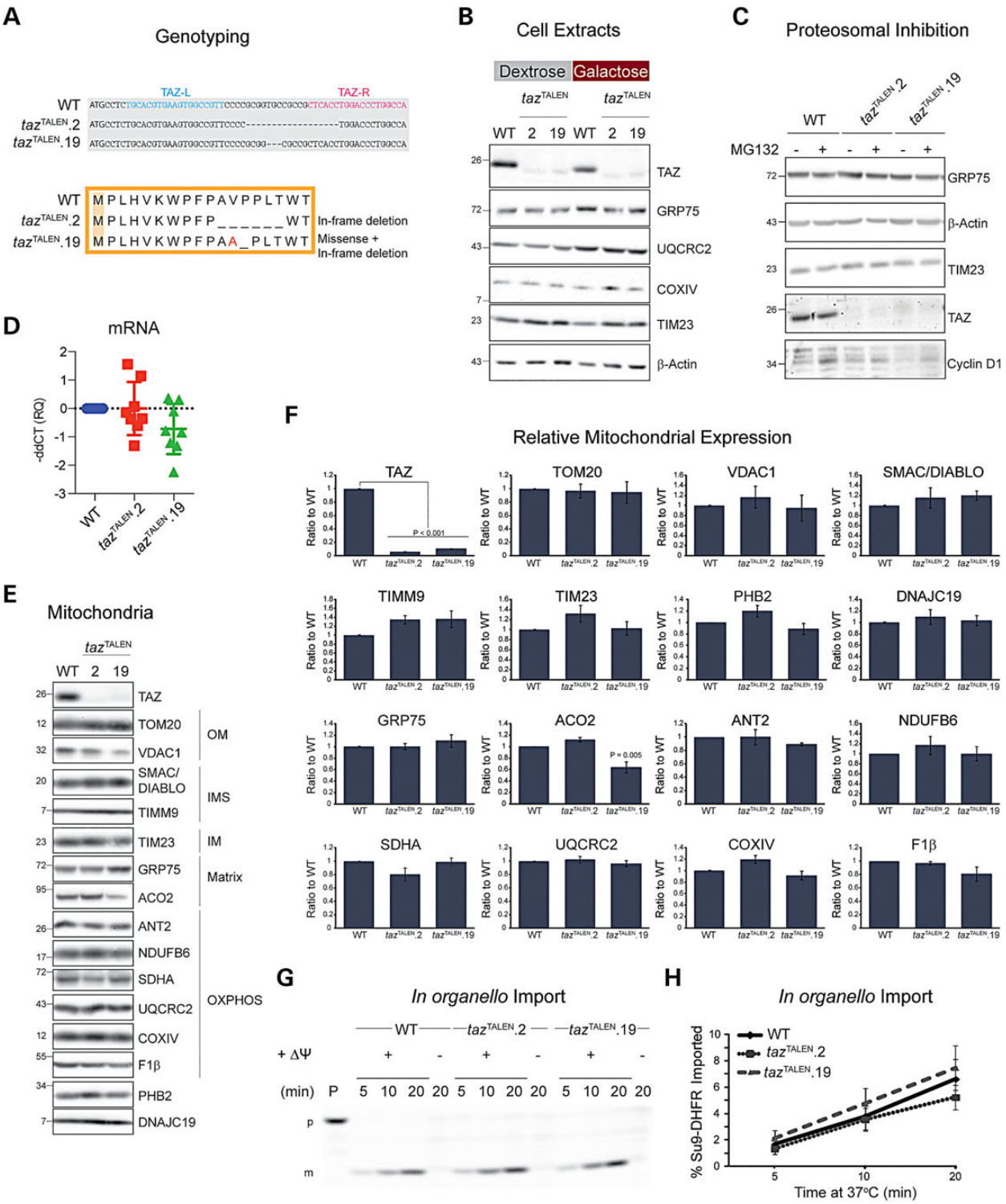

Figure 2. Generation of a BTHS cell culture model using TALEN-mediated genome editing. (**A**) TALEN-mediated disruption of TAZ in 293 Flp-In cells introduces nucleotide deletions that result in an in-frame deletion in *taz*^{TALEN}.2 and a missense and in-frame deletion in *taz*^{TALEN}.19. (**B**) Whole cell extracts from the indicated cells grown in dextrose- or galactose-based media were resolved by SDS–PAGE and immunoblotted. (**C**) WT 293 Flp-In and *taz*^{TALEN} cells were incubated for 4 h with 20 μM of the proteasome inhibitor, MG132. 40 μg of whole cell lysates were resolved by SDS–PAGE and immunoblotted for the indicated proteins. Cyclin D1, a target of the ubiquitin–proteasome pathway (35), is used as a positive control. (**D**) Relative mRNA level of TAZ in WT (293 Flp-In) and each *taz*^{TALEN} cell. Data were analyzed by the comparative C_T ($\Delta\Delta C_T$) method, represented as mean $\Delta\Delta C_T \pm$ SEM $n = 8$ relative to WT expression level, which was set to 0. (**E**) Mitochondria (50 μg) from the designated source were immunoblotted as listed. (**F**) Protein expression in (E) was quantified by densitometry and normalized to WT levels (mean ± SEM; $n = 3$). Significant differences are indicated. (**G**) *In organello* import of radiolabeled [^{35}S]-Su9-DHFR into WT 293 Flp-In and *taz*^{TALEN} mitochondria in the presence or absence of a membrane potential. Following import, mitochondria were osmotically ruptured, treated with trypsin, resolved by SDS–PAGE, and bands detected by phosphoimaging. P, precursor (5% of precursor protein + 100 μg mitochondria); p, precursor; m, mature. (**H**) The percentage of precursor imported at each time point was calculated (mean ± SEM; $n = 3$). See also Supplementary Material, Figure S1 and Table S1.

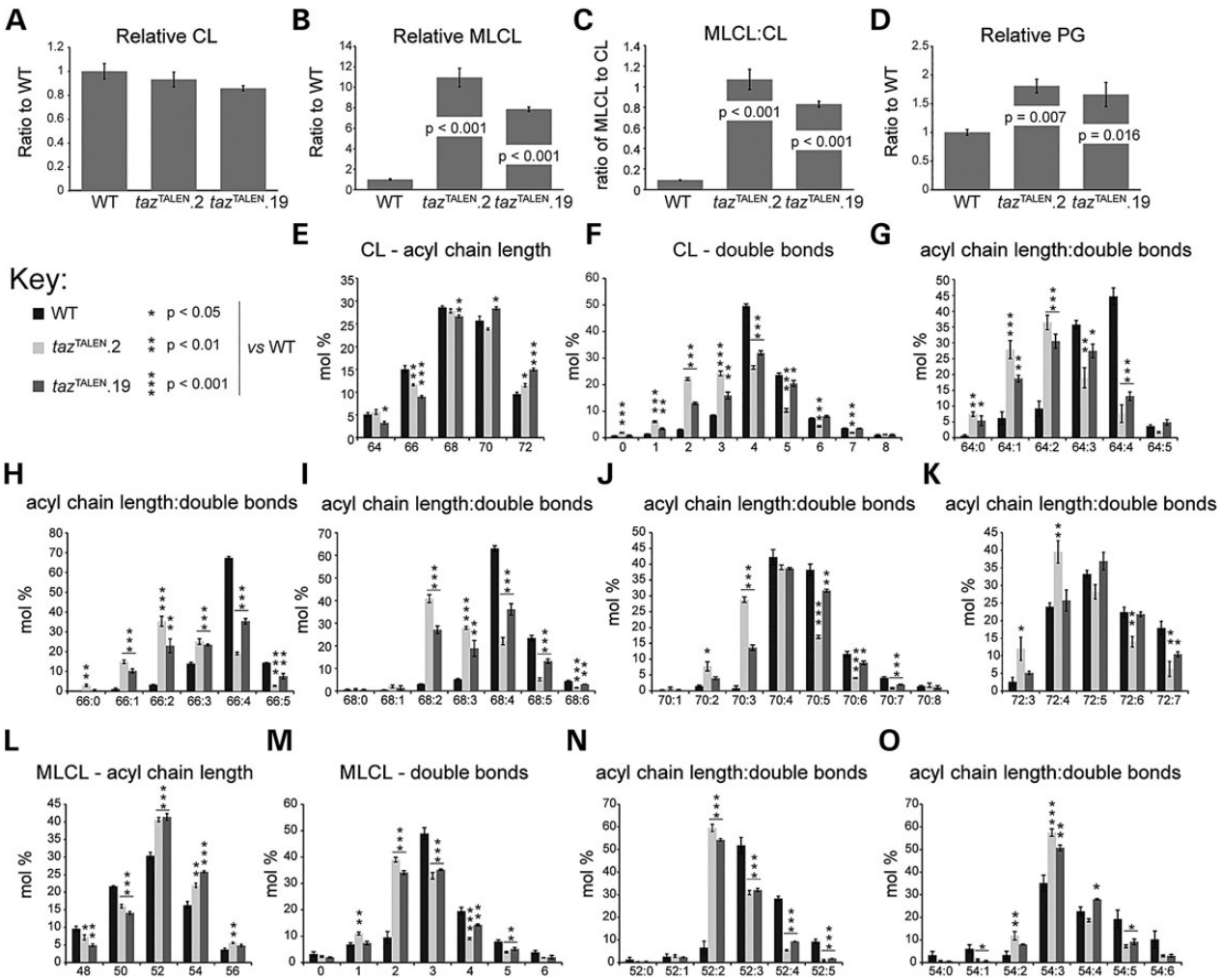

Figure 3. *taz*^{TALEN} cells have altered mitochondrial CL and MLCL profiles as determined by high-performance liquid chromatography-mass spectrometry. The relative amounts of CL (**A**), MLCL (**B**) and PG (**D**) was determined by high-performance liquid chromatography-mass spectrometry. (**C**) The ratio of MLCL:CL as determined from (A and B). The abundance of CL (**E**) and MLCL (**L**) of a given acyl chain length (E and L) or containing the indicated number of double bonds (**F** and **M**) was determined as a percentage of the total amount of CL or MLCL. The distribution of double bonds per acyl chain length for CL (**G–K**) and MLCL (**N** and **O**) expressed as a percent of the sum of all species of the indicated length. All data are the mean ± SEM ($n = 3$). Significant differences are indicated. See also Supplementary Material, Figures S2–S4.

length and saturation of phosphatidylcholine (PC) and phosphatidylethanolamine, two lipid classes that can be used by TAZ as acyl chain donors for MLCL re-acylation (16) (Supplementary Material, Figs S2–S4). Collectively, these results validate the *taz*^{TALEN} cells as new cellular BTHS models.

Mammalian TAZ is a membrane protein that assembles in high-molecular-weight complexes

Yeast Taz1 associates with the IMS-side of the IMM and OMM by virtue of a membrane anchor that extends into but not through the lipid bilayer (30). To determine if human TAZ is similarly membrane-associated, mitochondrial extracts from 293 Flp-In or C109 fibroblasts were sonicated and centrifuged to obtain the pellet, containing membrane-associated proteins, and the supernatant, containing soluble proteins. TAZ, like TIM23 and TOM20, was detected in the pellet fraction (Fig. 4A). Next, alkali extraction was performed. As expected, the integral proteins TIM23 and TOM20 were largely retained in the pellet whereas the peripheral cytochrome c was quantitatively released into the supernatant (Fig. 4B). Like yeast Taz1, human TAZ was steadily released into the supernatant as the pH increased, suggesting a similar mode of membrane association (Fig. 4C). Alternatively, analogous to succinate dehydrogenase subunit A (SDHA), TAZ membrane association may be determined by an interaction with a yet-to-be identified integral membrane protein.

As yeast Taz1 engages in a range of macromolecular complexes (30,37), the assembly of mammalian TAZ was examined by 2D blue native (BN)/SDS–PAGE. In both human and murine mitochondria, TAZ assembled in a range of complexes (Fig. 4D). In sum, these results demonstrate that mammalian TAZ associates with mitochondrial membranes and engages in macromolecular complexes in a manner that is highly reminiscent of its yeast ortholog.

Mammalian TAZ is highly protease resistant and localized to IMS-facing leaflets

Next, we determined the submitochondrial localization of TAZ. First, mitochondria from 293 Flp-In cells were titrated with

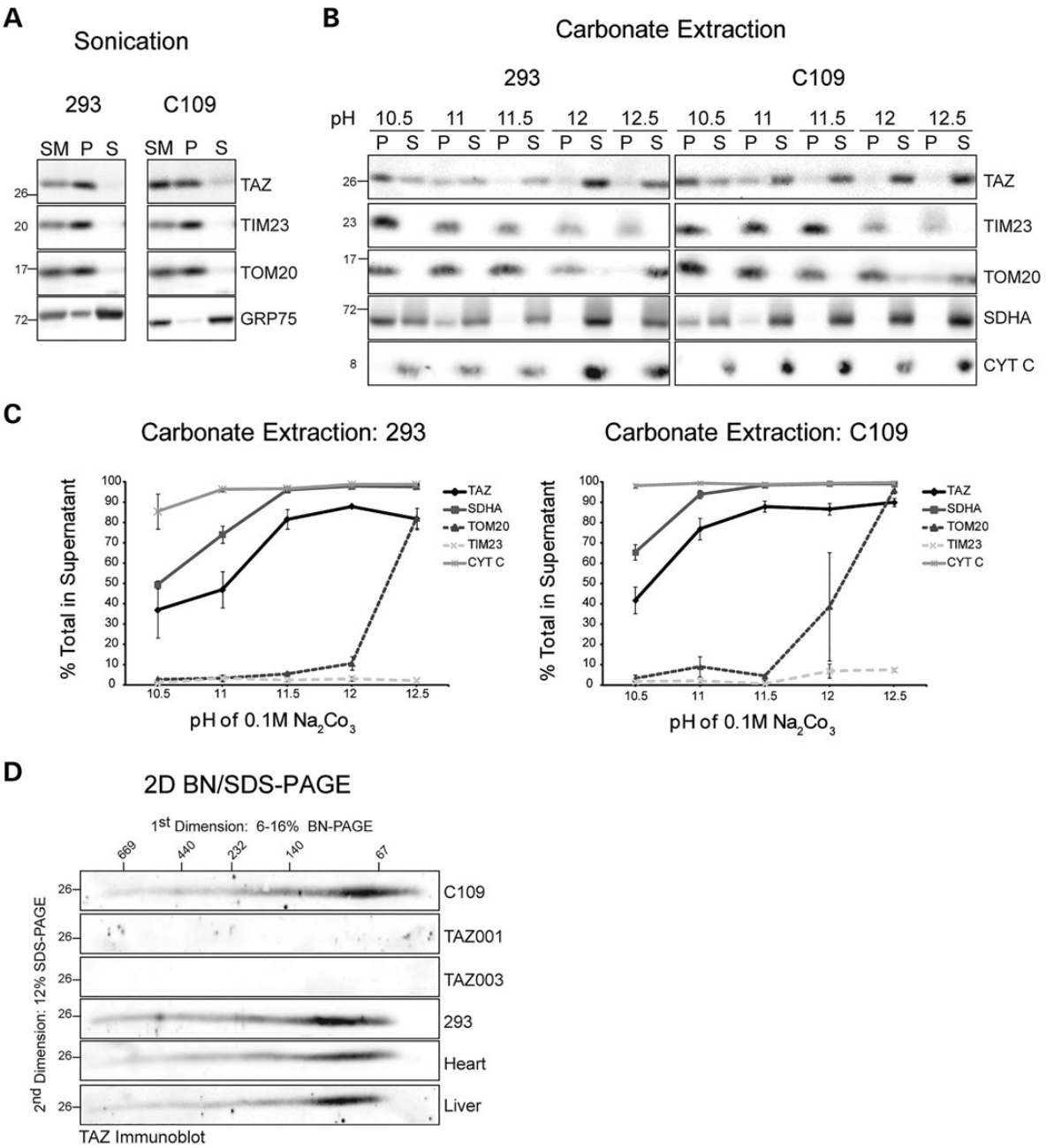

Figure 4. Membrane association and assembly of TAZ. (**A**) Mitochondria were sonicated and equal volumes of the pellet (P) and TCA-precipitated supernatant (S) fractions were immunoblotted as indicated. SM, starting material. (**B**) Mitochondria were incubated in 0.1 M Na_2CO_3 of the listed pH. Integral proteins (P) were separated from released proteins (S) by ultracentrifugation and equal volumes of each were immunoblotted as indicated. (**C**) Quantified band intensities of the P and S fractions were plotted as the percentage of total protein released into the supernatant for each pH (mean ± SEM; $n = 3$ (C109) or 4 (293)). (**D**) Mitochondria from control and BTHS fibroblasts (450 μg), 293 Flp-In cells (200 μg) and mouse heart and liver (200 μg) were solubilized with digitonin, separated by 2D BN/SDS–PAGE, and immunoblotted for TAZ.

increasing amounts of digitonin, causing the sequential release of soluble IMS proteins, soluble matrix proteins, membrane proteins of the OMM, and finally IMM-embedded proteins into the supernatant (Fig. 5A and B). The fractionation profile of human TAZ overlapped with both IMM and OMM proteins (Fig. 5B), suggesting that like yeast Taz1, human TAZ may associate with both the IMM and OMM (4,30,38).

Second, a protease-protection assay was performed to determine if human TAZ is associated with IMS-facing membranes as predicted based on results in yeast. In brief, human and murine mitochondria were incubated in iso-osmotic buffer, low osmotic buffer, or low osmotic buffer supplemented with detergent, with each permutation performed in the absence or presence of the nonspecific protease mixture, pronase E (Fig. 5C). Accordingly, OMM proteins facing the cytosol (e.g. TOM20) are accessible to added protease in each condition, residents of the IMS (TIM23; TIM23 is an IMM protein with a large domain exposed to the IMS) are degraded by added protease following osmotic rupture of the OMM (low osmotic buffer) and detergent solubilization, and matrix proteins (GRP75) are only degraded upon addition of detergent with protease. Like the matrix marker GRP75, in every source of mitochondria tested, mammalian TAZ was only

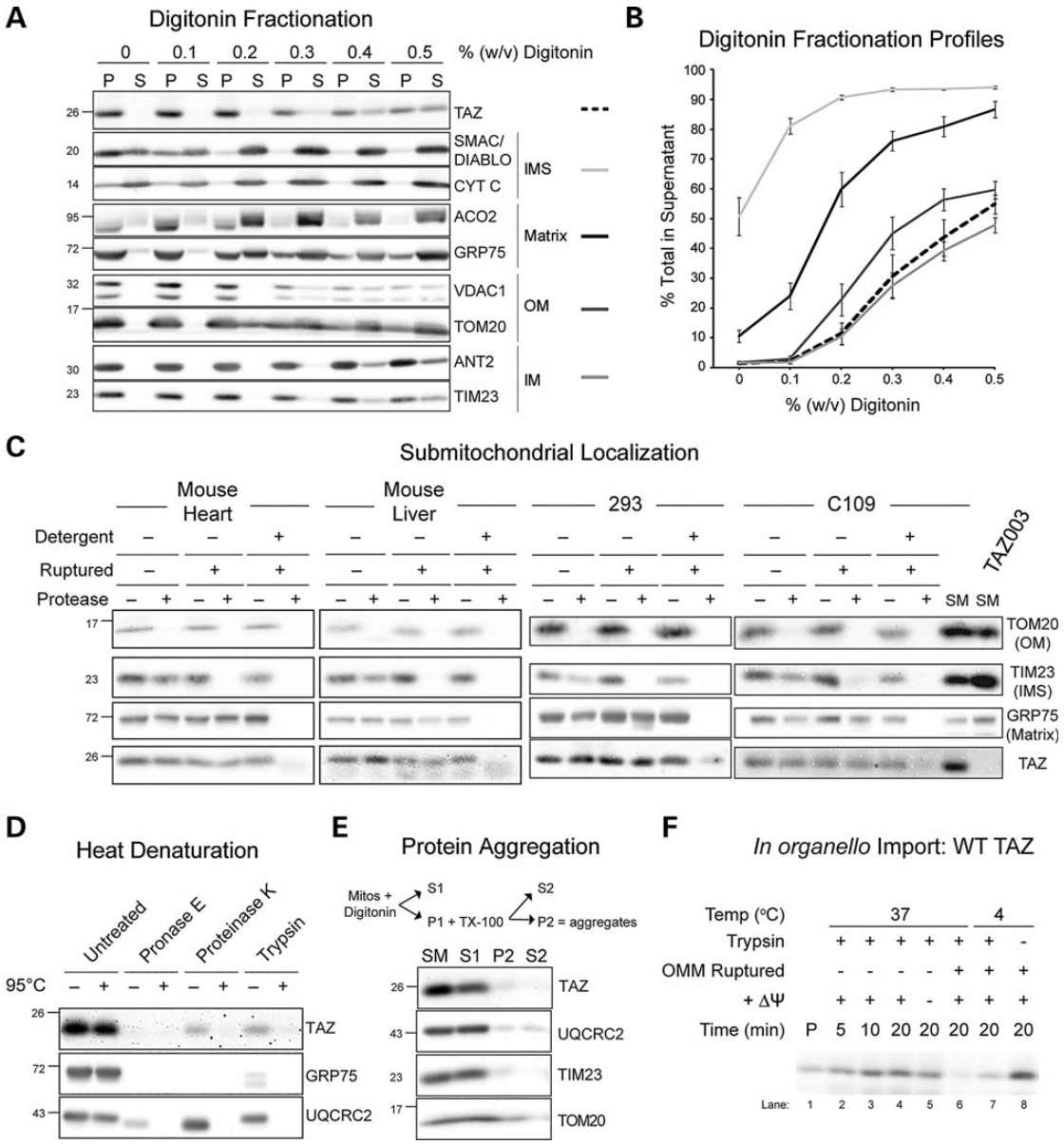

Figure 5. Mammalian TAZ is protease resistant and associates with IMS-facing leaflets. (**A**) Mitochondria were titrated with increasing amounts of digitonin to differentially solubilize mitochondrial compartments. After centrifugation, equal volumes of the pellet (P) and supernatant (S) fractions were resolved by SDS–PAGE and immunoblotted. (**B**) Quantified band intensities for two markers per compartment were combined and plotted as the percent detected in supernatant (mean ± SEM; $n = 7$). (**C**) Mitochondria, osmotically ruptured mitoplasts, or detergent-solubilized mitochondria from the indicated source were incubated without or with protease, resolved by SDS–PAGE, and immunoblotted. (**D**) Mitochondria were solubilized with 0.1% (v/v) SDS and where indicated, heated at 95°C for 5 min prior to adding pronase E, proteinase K or trypsin. Equal volumes of each sample were resolved by SDS–PAGE and immunoblotted. (**E**) Mitochondria were solubilized with digitonin and fractionated into a supernatant (S1) and pellet (P1) by centrifugation. Material not extracted by digitonin (P1) was further solubilized with TX-100 and separated into a supernatant (S2) and pellet (P2) by centrifugation. Fractions were resolved by SDS–PAGE and immunoblotted as indicated. (**F**) *In organello* import of radiolabeled [^{35}S]-TAZ into 293 Flp-In mitochondria at the indicated temperature in the presence or absence of a membrane potential. Following import, mitochondria were treated with trypsin, resolved by SDS–PAGE, and bands detected by phosphoimaging. Where indicated, mitochondria were osmotically ruptured in the presence or absence of trypsin. P, precursor (5% of precursor protein + 100 μg mitochondria).

degraded by pronase after detergent solubilization. These results thus suggest that mammalian TAZ is localized to the matrix-facing leaflet of the IMM, the opposite side of the IMM as yeast Taz1.

This conclusion, however, is predicated on TAZ being sensitive to protease. Thus, another potential explanation for the observed pattern is that perhaps TAZ adopts a highly protease-resistant fold that becomes accessible to proteolytic cleavage only in the presence of detergent. To test the idea that TAZ is protease-resistant, we compared its sensitivity to proteases upon addition of detergent with or without prior heat denaturation (Fig. 5D). When solubilized with SDS, heat denaturation increased the sensitivity of TAZ to degradation by each protease. One potential explanation for the resistance of TAZ to proteolytic degradation is that it forms aggregates. However, using a sequential detergent solubility assay where TAZ was readily solubilized with digitonin (protein aggregates resist solubilization even when re-extracted with TX-100), TAZ does not form protein aggregates (Fig. 5E).

In light of TAZ's protease resistance, the assays performed cannot conclusively establish the topology of membrane-associated TAZ. Therefore, we performed an *in organello* import assay in which radiolabeled TAZ precursor was incubated with WT mitochondria in the presence or absence of a membrane potential and non-imported precursor removed with trypsin (Fig. 5F). Import of TAZ was time-dependent but membrane potential-independent. The TAZ precursor was not processed upon import consistent with the failure of most *in silico* programs (Supplementary Material, Table S2) to predict a mitochondrial presequence cleavage site. Critically, ^{35}S-TAZ precursor was readily degraded by trypsin following incubation with mitochondria on ice and disruption of the OMM (compare lanes 7 and 8). Finally, following import in the presence of a membrane potential, disruption of the OMM in the presence of trypsin drastically decreased the ^{35}S-TAZ detected (lane 6). Thus, the protease resistance of TAZ observed at steady state occurs after it is imported into the mitochondrial IMS.

To gain further insight into the topology of TAZ, epitopes tags were added to either termini of TAZ (CNAP-TAZ and TAZ-3XFLAG for NH_2- or COOH-terminal tagged TAZ, respectively) (Fig. 6A). Upon transfection into the *taz*^{TALEN}.19 cell line, each construct was expressed similar to untagged WT TAZ (Fig. 6B) and importantly, rescued the altered MLCL:CL ratio of this TAZ-deficient model (Fig. 6C and D). The sensitivity of the appended epitope tags to proteolytic degradation was determined in intact mitochondria, following OMM rupture, or in the presence of detergent. Like the IMS marker TIM23, which is anchored to the IMM but exposes a large domain in the IMS, the NH_2-terminal epitope of CNAP-TAZ became sensitive to added protease when the OMM was disrupted (Fig. 6F). In contrast, 3XFLAG added to the COOH terminus of TAZ was resistant to proteolytic degradation unless detergent was included (Fig. 6F). Thus, either the COOH terminus of TAZ is in the matrix, implying that TAZ has a membrane-spanning domain contrary to expectations based on its alkali extraction profile (Fig. 4B and C), or alternatively, the added tag is incorporated in the core protease-resistant structure of TAZ. To distinguish between these two possibilities, we transfected the *taz*^{TALEN}.19 cell line with TAZ harboring a COOH-terminal APEX2 tag (39,40). APEX2 encodes an engineered ascorbate peroxidase that can be used in electron microscopy studies to localize a tagged protein (39,40). TAZ-APEX2 was expressed normally and functional based on the restored MLCL:CL ratio (Fig. 6B–D). When *taz*^{TALEN}.19 cells expressing TAZ-APEX2 were reacted with 3,3′-diaminobenzidine (DAB), in the presence of H_2O_2, electron micrographs revealed reaction products in and around the mitochondrial IMS (Fig. 6G). Conversely, DAB staining of *taz*^{TALEN} cells expressing untagged TAZ (control) revealed no staining of the IMS. Our combined results indicate that mammalian TAZ adopts a highly protease-resistant structure following its import into the mitochondrial IMS where it non-integrally associates with mitochondrial membranes with both termini exposed to the IMS.

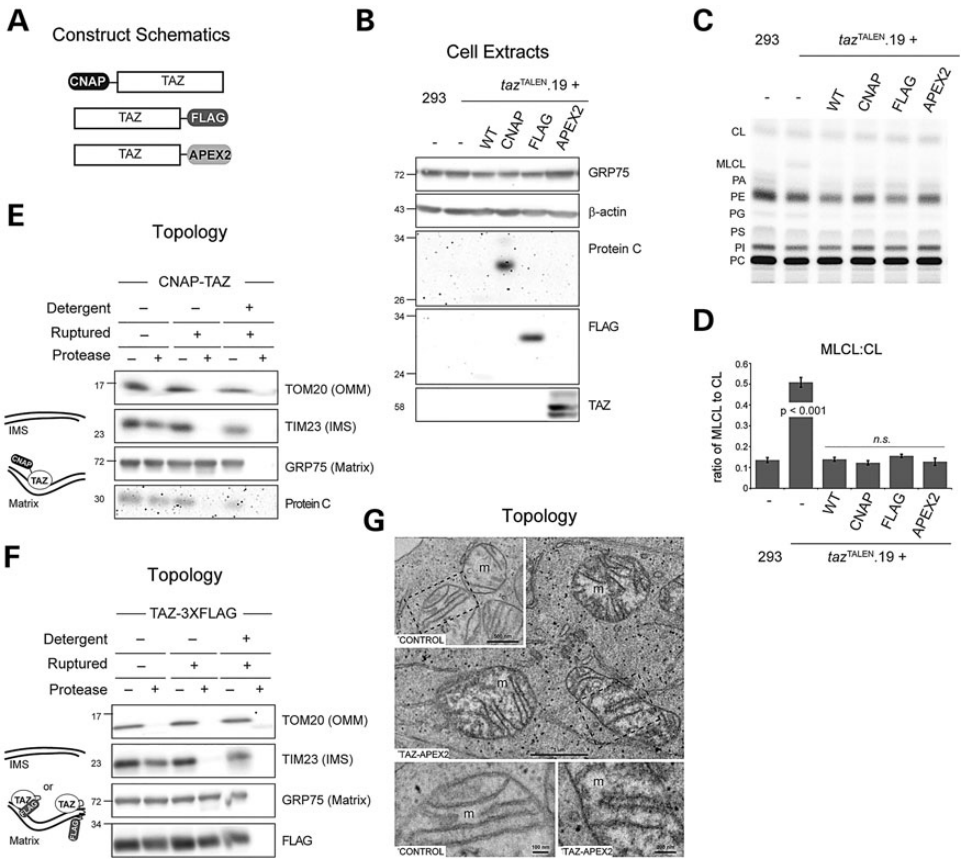

Figure 6. Both termini of TAZ are in the IMS. (**A**) Cartoon of epitope tagged TAZ constructs. (**B**) Whole cell extracts (30 μg) were immunoblotted for the indicated proteins. (**C**) Phospholipids from the indicated cells were labeled with $^{32}P_i$ and separated by TLC. (**D**) Quantification of the MLCL:CL ratio (mean ± SEM; $n = 3$). Significant differences compared with WT 293 Flp-In cells were determined by one-way ANOVA. n.s. = differences not significant. (**E** and **F**) The protease accessibility of epitope tags added to the NH_2 (E) or COOH (F) termini of TAZ was determined as in Figure 5C. (**G**) *taz*^{TALEN}.19 cells overexpressing WT or TAZ-APEX2 were labeled *in vivo* with H_2O_2 and DAB followed by OsO_4 and EM imaging. Scale bars are provided in each panel.

The R57L allele encodes an unstable protein

TAZ003 fibroblasts harbor an R57L missense mutation that was previously classified in yeast (K65L) as a temperature-sensitive allele (Fig. 7A) (20,32). As such, the inability to detect TAZ in TAZ003 cells could provide evidence that like in yeast, the R57L allele is intrinsically unstable. To determine if the R57L allele encodes an unstable polypeptide, we re-introduced into the two *taz*^{TALEN} cell lines WT TAZ, R57L, and an H69Q TAZ mutant that in yeast encodes a catalytically null polypeptide (32). The 5 and 6 subclones that were isolated per construct per parental cell line displayed little variability in TAZ expression for a given TAZ allele (Fig. 7B). Consistent with the possibility that the R57L allele is intrinsically unstable, its steady-state expression in clones from both *taz*^{TALEN} cells was dramatically reduced compared with WT TAZ-expressing cells. The reduced expression was not reflected at the transcript level (Fig. 7C), did not result from impaired import into the mitochondrial IMS (Fig. 7D), and was not restored upon proteosomal inhibition (Fig. 7E and Supplementary Material, Fig. S5A). Moreover, when cytosolic protein synthesis was inhibited with cycloheximide, R57L had a much shorter half-life ($t_{1/2}$) than WT TAZ (Fig. 7F and Supplementary Material, Fig. S5B). Thus, as previously characterized in a yeast BTHS model (32), the R57L BTHS variant encodes an unstable protein.

The H69Q allele is catalytically null

The H69Q mutation disrupts a highly conserved HXXXXD acyltransferase motif. When modeled in yeast, the equivalent H77Q mutation results in a protein that behaves biochemically and

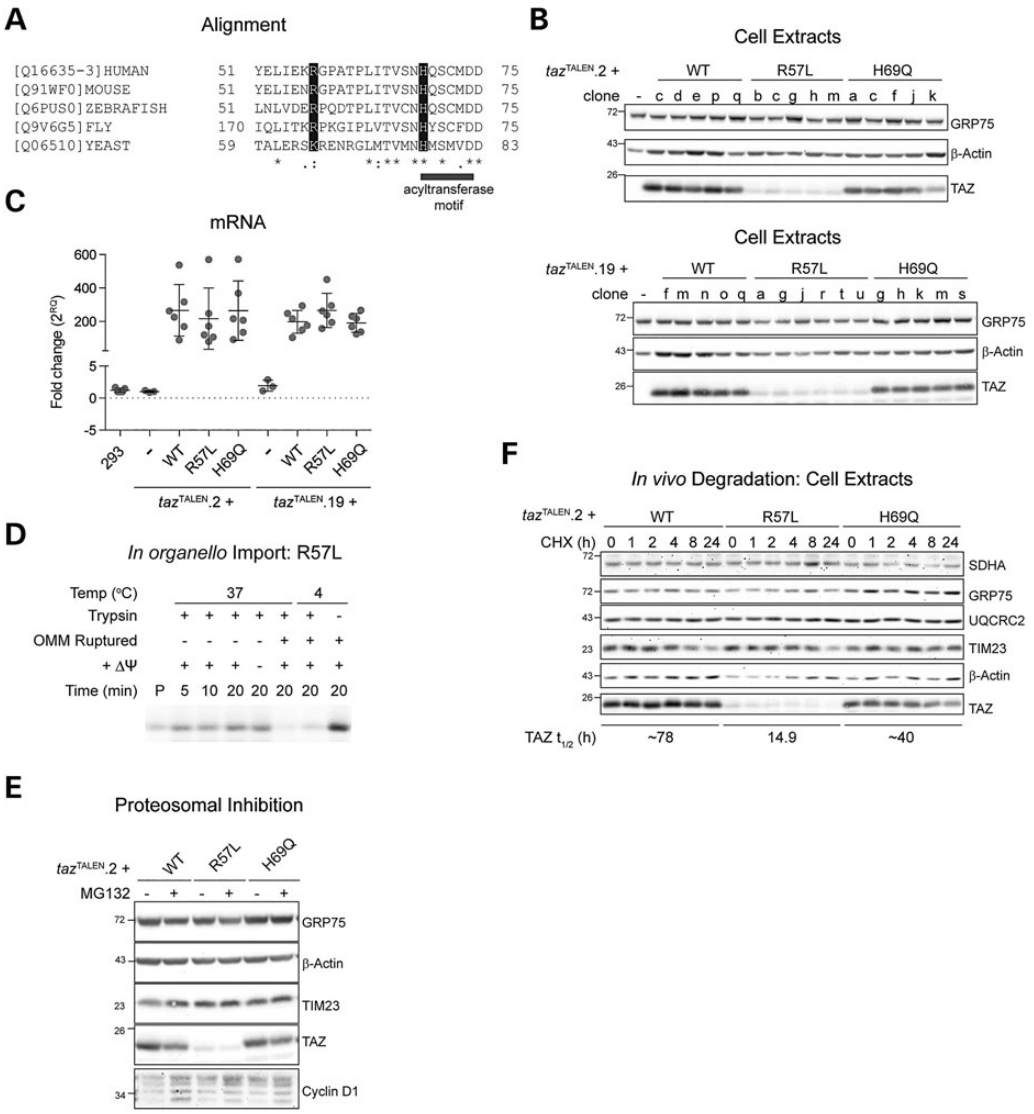

Figure 7. The R57L allele is highly unstable. (**A**) Sequence alignment of TAZ from the indicated species encompassing human Arg57 and His69 (*white* face on black background) and the HXXXXD motif (underlined). (**B**) Whole cell extracts (20 μg) from 5 to 6 clones transfected with the indicated TAZ alleles were immunoblotted. (**C**) Relative mRNA level of TAZ analyzed by the comparative C_T ($\Delta\Delta C_T$) method, represented as mean fold change ($2^{\Delta\Delta C_T}$) ± SD $n \geq 4$ relative to 293 Flp-In TAZ expression. (**D**) *In organello* import of radiolabeled precursor R57L TAZ into freshly isolated 293 Flp-In mitochondria as described in Figure 5F. (**E**) *taz*^{TALEN} cells overexpressing WT, R57L and H69Q alleles were incubated for 4 h with 20 μM of the proteasome inhibitor, MG132. 40 μg of whole cell lysates were resolved by SDS–PAGE and immunoblotted for the indicated proteins. (**F**) Whole cell extracts (20 μg) were collected after incubation with cycloheximide for the indicated times, and the amount of TAZ remaining assessed by immunoblot. The half-lives of the indicated TAZ alleles were calculated using the mean of five individual repetitions. See also Supplementary Material, Figure S5.

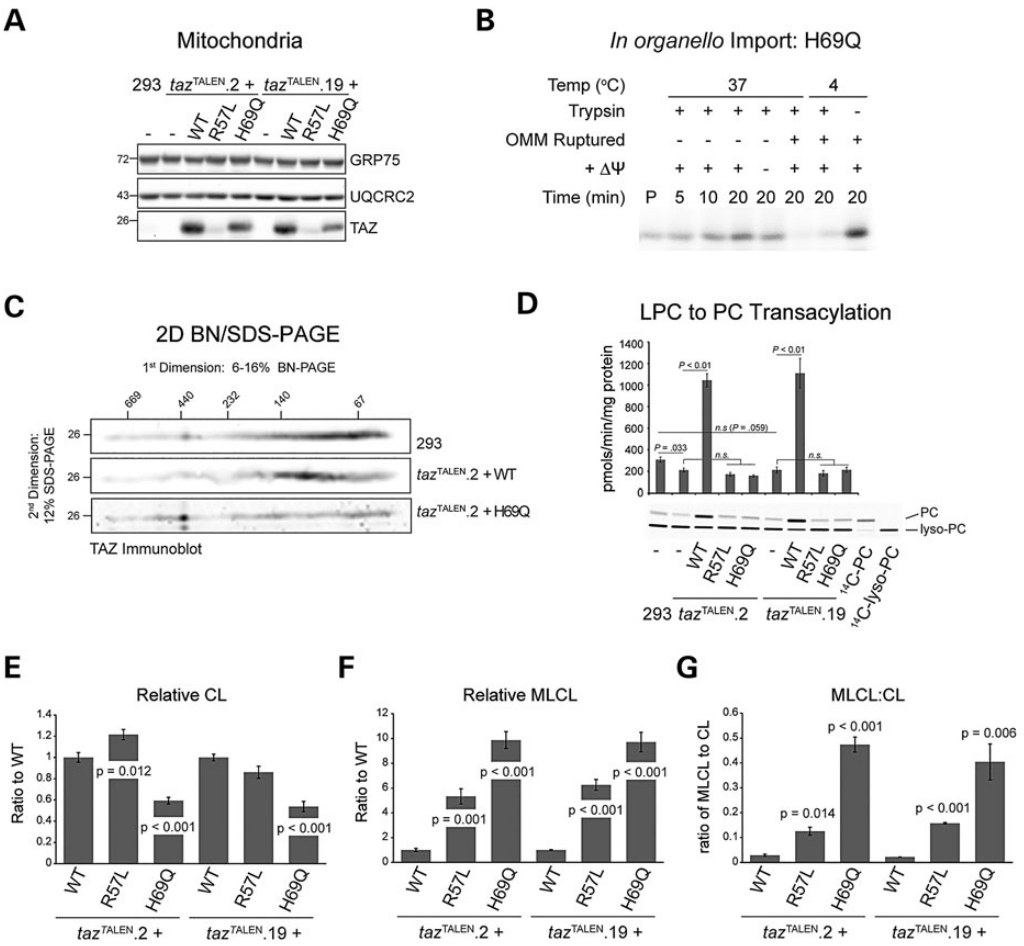

Figure 8. The H69Q mutant is catalytically dead. (**A**) Mitochondria (20 μg) from 293 Flp-In, *taz*^{TALEN} and *taz*^{TALEN} cells overexpressing WT, R57L and H69Q alleles were immunoblotted as indicated. (**B**) *In organello* import of radiolabeled precursor H69Q TAZ into freshly isolated 293 Flp-In mitochondria as described in Figure 5F. (**C**) Assembly of H69Q as determined by 2D BN/SDS–PAGE. (**D**) Lyso-PC to PC transacylase activities were determined in mitochondria isolated from 293 Flp-In, *taz*^{TALEN} and *taz*^{TALEN} cells overexpressing the indicated TAZ alleles (mean ± SEM, $n = 3$). Significant differences are indicated. n.s., not significant. The relative amounts of CL (**E**) and MLCL (**F**), and the subsequent MLCL:CL ratio (**G**), in *taz*^{TALEN} cells overexpressing WT, R57L and H69Q were determined as previously described. See also Supplementary Material, Figure S5.

cell biologically like WT Taz1 but that is completely devoid of transacylase activity (32). As expected, expression of H69Q in whole cell extracts (Fig. 7B) and isolated mitochondria (Fig. 8A) was similar to WT TAZ. The H69Q allele was imported into the mitochondrial IMS (Fig. 8B) and assembled in complexes (Fig. 8C and Supplementary Material, Fig. S5C) just like WT TAZ. The preserved complex formation of the H69Q mutant indicates that TAZ assembly is insensitive to increased MLCL or changes in CL acylation. To directly measure the transacylase activity of WT and mutant TAZ, isolated mitochondria were incubated with ^{14}C-labeled lyso-PC and its conversion to PC monitored (Fig. 8D). Overexpression of WT TAZ resulted in dramatically increased transacylase activity. In stark contrast, mitochondria overexpressing H69Q (or R57L) lacked any detectable transacylase activity above background. Finally, while WT TAZ restored the MLCL:CL ratio of both *taz*^{TALEN} cell lines to normal, overexpression of the H69Q mutant did not (Fig. 8E–G). Therefore, the H69Q variant encodes a catalytically inactive polypeptide in both mammals and yeast. Intriguingly, overexpression of the R57L mutant, which was devoid of transacylase activity *in vitro* (Fig. 8D) did partially improve the MLCL:CL ratio of both *taz*^{TALEN} cell lines *in vivo* (Fig. 8E–G) indicating that prior to its degradation, it retained some residual catalytic activity. Consistently, the R57L allele was still assembled normally (Supplementary Material, Fig. S5C). Collectively, these results suggest that the LOF mechanisms that underlie certain missense mutations are conserved in yeast and mammalian BTHS models.

Discussion

We have determined that CL remodeling is organized in topologically similar ways in mammals and yeast. Like in yeast, mammalian TAZ is localized to the IMS-facing leaflets of the OMM and IMM. Thus, the main determinant of the final CL acyl chain pattern, TAZ, resides on the opposite side of the IMM as the CL biosynthetic machinery. In yeast, the lipase that functions upstream of Taz1, Cld1, is peripherally associated with the matrix side of the IMM (41). At present, the identity and detailed localization of the mammalian lipase(s) that functions upstream of human TAZ to initiate CL remodeling has not been defined. The rationale for the localization and topology of TAZ-based CL remodeling in yeast and mammals is presently unclear but is presumed to be important for it to function properly. Notably, besides dictating the final acyl chain pattern of CL, the physiological functions of this conserved remodeling pathway remain elusive (42).

Overall, our work suggests that human and yeast TAZ, whose polypeptides are only 18% identical and 41% conserved, are remarkably similar biochemically. Not only are their submitochondrial localizations the same, yeast and mammalian TAZ also interact with mitochondrial membranes in a similar manner which in yeast involves a membrane anchor that extends into but not completely through the lipid bilayer (30). Further, both yeast and mammalian TAZ assemble in a range of complexes that appear qualitatively quite comparable (37). Previously, we demonstrated that yeast Taz1 does not associate with itself but does interact with the ATP synthase as well as the major mitochondrial ADP/ATP carrier, Aac2 (37). Thus, it is possible that these interactions will be evolutionarily conserved. However, it is important to mention that the vast majority of the yeast Taz1 interactome remains undocumented and the noted interactions between yeast Taz1 and the ATP synthase or Aac2 are clearly sub-stoichiometric. The composition of all of the mammalian TAZ-associated complexes is similarly unknown but is something we are actively investigating.

Critically, another feature shared between yeast and mammalian TAZ are the LOF mechanisms associated with distinct pathogenic mutations. Using a novel BTHS cell model, the LOF mechanism for the two tested pathogenic mutations were conserved as modeled in yeast or human TAZ. In patient-derived TAZ003 cells, the protein product of the R57L allele is undetectable. When overexpressed in *taz*^{TALEN} cells, the R57L mutant localized properly and assembled normally (Supplementary Material, Fig. S5A–C), but accumulated to a much lesser extent and had a significantly shorter half-life than WT TAZ. The corresponding yeast mutant, K65L, is a temperature-sensitive allele that becomes unstable and loses activity at non-permissive temperature (32). Interestingly, even though the R57L allele lacked *in vitro* activity, its overexpression did improve the MLCL:CL ratio in both *taz*^{TALEN} cells (Fig. 7G). Therefore, small molecules capable of stabilizing the R57L mutant could increase its activity and thus represent viable therapeutic options. Importantly, dysfunctional conservation extends to the H69Q mutation. In yeast, the corresponding H77Q mutant is identical to WT Taz1 in every way tested except that it is devoid of transacylase activity (32). As predicted from yeast, the H69Q mutant allele closely resembled WT TAZ except that it was catalytically null.

TAZ is a promiscuous transacylase that can utilize a range of lyso-lipid substrates and phospholipid acyl chain donors. Moreover, TAZ itself lacks intrinsic acyl chain specificity which raises the obvious question of how a non-specific enzyme can generate CL that typically has a specific collection of acyl chains. Recent experiments have suggested that the physical state of phospholipid membranes can affect the substrate specificity of TAZ. Under experimental conditions that mimic high membrane curvature, have an increased proportion of non-bilayer lipids, or perturbed bilayer states, TAZ gains the capacity to generate the physiologically relevant CL molecular form that contains four attached 18:2 linoleic acids (43). In mitochondria, such privileged lipid domains may be delineated by the recently described prohibitin/DNAJC19 complexes (28). The ring-shaped prohibitin complexes, composed of PHB1 and PHB2 subunits and including DNAJC19 (28), form protein and lipid scaffolds within the IMM that contribute to cristae morphogenesis and cell proliferation (44). Surprisingly, knockdown of either PHB2 or DNAJC19, which do not interact with TAZ, changes the acyl chain pattern of CL similar to TAZ depletion (28). Depletion of either protein with TAZ does not prevent the accumulation of MLCL. These findings suggest that PHB/DNAJC19 complexes participate in CL remodeling after the process is initiated. Since MLCL does not accumulate, TAZ is still active when PHB2 or DNAJC19 expression is reduced. Although both completely traverse the IMM bilayer, the majority of the DNAJC19 polypeptide resides in the matrix. Thus, how PHB/DNAJC19 complexes could modulate TAZ specificity remains unclear based on the submitochondrial localization and interfacial membrane association of TAZ as defined previously in yeast and here in mammals. Given our placement of mammalian TAZ on the IMS-leaflet of the IMM, it is tempting to speculate that PHB/DNAJC19 complexes sequester TAZ within membrane domains with physical properties (high membrane curvature) that confer acyl chain specificity to TAZ. While the exact details of how PHB/DNAJC19 complexes modulate the specificity of TAZ-mediated CL remodeling is undefined, the functional relationship between PHB/DNAJC19 complexes and TAZ is underscored by the fact that mutations in DNAJC19 result in DCMA, a disease that shares many clinical features with BTHS (25,26). Our results thus establish a framework to dissect the functional relationship between PHB/DNAJC19 complexes and TAZ which may in turn reveal the basis for the shared and distinct phenotypes of BTHS and DCMA.

Materials and Methods

Molecular biology

The human TAZ ORF lacking exon 5 was amplified by PCR using cDNA from HeLa cells and subcloned first into pBSK (Stratagene) and then into pcDNA5/FRT (Invitrogen). The R57L and H69Q mutations were introduced into the parental pcDNA5/FRThTAZ plasmid via overlap extension (45). TAZ with an NH_2-terminal CNAP tag (46) or COOH-terminal 3XFLAG or APEX2 tags were introduced into the parental pcDNA5/FRThTAZ plasmid via overlap extension (45). For TAZ-APEX2, pcDNA3APEX2-NES (40), a gift from Alice Ting (Addgene plasmid # 49386), was used as template. For *in vitro* transcription/translation, WT TAZ and the R57L and H69Q alleles were subcloned into pSP64. The sequence of every construct was verified by DNA sequencing. The TALEN binding pair recognizes sequences in TAZ exon1 that are separated by 16 nucleotides and immediately downstream of the start site (Life Technologies). The two constructs, which are fused to the truncated Fok1 nuclease, were subcloned into pcDNA3.1 and pEF6/V5-HisA (Life Technologies) generating pcDNA3TAZ1-R and pEF6ATAZ1-L, respectively.

Cell culture

All cells were grown at 37°C, 5% CO_2. Control (C109) and BTHS patient fibroblasts (TAZ001 and TAZ003) (20) were maintained in DMEM (Cellgro) containing 10% fetal bovine serum (FBS, Hyclone), 2 mM L-glutamine (Gibco), and 50 units/l penicillin-streptomycin (Gibco). HEK293 Flp-In cells (Invitrogen) were grown in DMEM containing 10% FBS, 2 mM L-glutamine and 100 μg/ml zeocin (Invitrogen). To establish a BTHS cell model, 293 Flp-In cells grown in medium lacking antibiotic but supplemented with 50 μg/ml uridine, were transfected with a 1:1 ratio of pCDNA3-TAZ1-R and pEF6ATAZ1-L using FuGENE 6 (Promega), selected with 0.5 mg/ml G418 and 5 μg/ml blasticidinS (Cellgro) for 1 week, and single colonies isolated by ring cloning. Individual clones were maintained in the same medium as used for the parental 293 Flp-In cells and the inclusion of uridine found to not be essential. Whole cell extracts derived from candidate clones were harvested and analyzed by SDS–PAGE and immunoblot. Stable *taz*^{TALEN} rescue cell lines were generated by co-transfecting the two *taz*^{TALEN} cell lines with pOG44 (expressing

the Flp-recombinase) and the relevant pcDNA5/FRT plasmid (WT, CNAP-TAZ, TAZ-3XFLAG, TAZ-APEX2, R57L, H69Q) at a ratio of 9:1 using FuGENE 6. Transfected cells were selected using 200 μg/ml hygromycin B (Invitrogen), individual clones recovered by ring cloning, expanded and screened by immunoblot. Equal numbers of individual clones per construct were combined to establish a pooled clonal population that was then used in all subsequent analyses. Each pooled population was derived from at least five individual clones except for taz^{TALEN}.19 overexpressing CNAP-TAZ which was established from three clones. Mycoplasma contamination was routinely monitored and not detected.

Purification of recombinant human TAZ

The entire open reading frame of *TAZ* lacking exon 5 was cloned into the pET28a vector (Novagen) downstream of the 6× His tag, induced at 37°C for 4 h with 1 mM IPTG in C41 (DE3) *Escherichia coli*, and inclusion bodies separated from native protein extracts by centrifugation at 22 000 × *g* for 1 h at 4°C. Lipids and debris were removed from the inclusion bodies by resuspending the pellet with 7–10 ml of wash buffer (50 mM Tris–HCl, pH 7.0, 2.5 mM EDTA, 1 M urea, 1% (v/v) Triton X-100) per gram of cells using a dounce homogenizer followed by centrifugation at 22 000 × *g* for 30 min at 4°C. This wash step was repeated three times until the supernatant was clear. A final wash was performed using wash buffer lacking urea and Triton X-100. The final recovered protein pellet was resuspended using a dounce homogenizer with 4 ml of extraction buffer (50 mM HEPES–KOH, pH 7.5, 5 mM EDTA, 8 M guanidine-HCl, 2 mM β-mercaptoethanol) per gram of cells and clarified by centrifugation at 100 000 × *g* for 1 h at 4°C. The solubilized inclusion bodies were mixed 1:1 with ddH_2O, His_6-TAZ purified using Ni^{2+} agarose (Qiagen) and bound material recovered under denaturing conditions.

Antibodies

Custom mAbs against human TAZ-ex5 were produced by Genscript using purified recombinant protein as antigen. Three hybridomas—2C2C9, 3D7F11 and 2G3F7—that secrete TAZ-reactive antibodies were established. Antibodies against the following proteins were: GRP75 (Antibodies Inc. 75-127); β-actin (A5441) and TIMM9 (WH0026520M1) (Sigma); topoisomerase I (Developmental Studies Hybridoma Bank CPTC-TOP1-1-S); calreticulin 3 (sc-134295) and TOM20 (sc-11415) (Santa Cruz); HLA-B (Epitomics 2389-1); TIM23 (611332), CYCS (556433), SMAC/DIABLO (612246) and cyclin D1 (556470) (BD); UQCRC2 (ab14745), ACO2 (ab129069), VDAC1 (ab15895) and COX4 (ab16056) (Abcam); SDHA (Invitrogen 4592000); PHB2 (BioLegend 611802); DNAJC19 (ProteinTech 12096-1-AP); and NDUFB6 (Molecular Probes, discontinued). F1β was a kind gift from Dr Peter Pedersen (Johns Hopkins School of Medicine) and the ANT2/5H7 (47) antibody was raised against the yeast ADP/ATP carrier, Aac2, but conveniently cross-reacts with human and murine ANT2. Goat anti-rabbit or mouse secondary antibodies conjugated to horseradish peroxidase were also used (31460 and 62-6520; Pierce).

Whole cell extraction

Confluent culture dishes were washed twice with ice-cold PBS and lysed with RIPA lysis buffer (1% (v/v) Triton X-100, 20 mM HEPES–KOH, pH 7.4, 50 mM NaCl, 1 mM EDTA, 2.5 mM $MgCl_2$, 0.1% (w/v) SDS) spiked with 1 mM PMSF for 30 min at 4°C with rotation. Insoluble material was removed by centrifugation for 30 min at 21 000 × *g* at 4°C, the supernatant collected, and protein quantified using a bichichronic acid (BCA) assay (Pierce).

Immunoblotting

SDS–PAGE and immunoblotting was performed as previously described (48). Images were captured with a Fluorchem Q (Cell Biosciences, Inc.) quantitative digital imaging system and quantitation performed using the indicated software. Images were processed in Adobe Photoshop with only linear adjustments in contrast and brightness and assembled in Adobe Illustrator.

Preparation of subcellular fractions

Fibroblasts and 293 Flp-In cells were seeded onto four 150 × 25 mm tissue-culture dishes and allowed to expand to confluency. Two days prior to mitochondrial isolation, the cells were switched from dextrose- to galactose-based media (DMEM without glucose, Gibco; supplemented with 10 mM galactose, Sigma). Mitochondria were isolated on ice (with ice-cold buffers) using a protocol adapted from (49). Briefly, after aspirating spent media from dishes, cells were scraped off in PBS and centrifuged at 600 × *g* for 10 min. After washing the cells once more with PBS, the pelleted cells were resuspended in 3 ml isolation buffer (IB_C, 10 mM Tris–MOPS, 1 mM EGTA/Tris, pH 7.4, 200 mM sucrose) and homogenized with 40–45 strokes in a motor-driven tightly fitting Teflon Potter-Elvehjem at 1600 rpm. Cell lysates were then centrifuged twice at 600 × *g* for 10 min; the resulting pellet is the nuclear fraction. Mitochondria were recovered from the supernatant by centrifugation at 7000 × *g* for 10 min. The mitochondrial pellet was resuspended to a volume that fits a 1.5 ml microcentrifuge tube; after an additional 7000 × *g* spin, a 10 000 × *g* clarifying spin was performed to obtain crude mitochondria. The supernatant from the prior 7000 × *g* spin contains cytosolic, lysosomal and ER fractions which were further sub-fractionated as follows. Lysosomes were pelleted after a 20 000 × *g* spin for 30 min and resuspended in a residual amount of IB_C. The remaining supernatant was centrifuged at 40 000 × *g* for another 30 min to obtain plasma membranes. Further centrifugation of the obtained S40 (100 000 × *g* for 1 h) resulted in the isolation of ER (pellet) and cytosolic fractions (supernatant). Heart and liver mitochondria from 10- to 12-week-old female FVB mice were isolated on ice using a protocol adapted from (50,51). Briefly, tissues were rinsed with ice-cold CP1 (100 mM KCl, 50 mM MOPS, pH 7.4, 5 mM $MgSO_4$, 1 mM EGTA, 1 mM ATP), minced with scissors and washed several times with CP1 before resuspension in CP2 (CP1 supplemented with 2 mg/ml BSA). Tissues were then homogenized using a Polytron (three 2.5 s pulses on medium setting; Fisher PowerGen 1000 large bore homogenizer). The homogenate was centrifuged at 580 × *g* for 7 min at 4°C and the resultant supernatant contained either liver mitochondria or in the case of heart tissue, subsarcolemmal mitochondria (SSM), while the pellet contained heart interfibrillar mitochondria (IFM). Liver and SSM supernatants were repeatedly centrifuged at 580 × *g* until there were no visible cell/debris pelleting. A final clarifying spin at 3000 × *g* for 7 min was performed before resuspending the mitochondrial pellets in KME (100 mM KCl, 50 mM MOPS, 1 mM EGTA). To extract IFM mitochondria, the pellet was resuspended in CP1 containing 5 mg trypsin per gram tissue with mixing, for 10 min on ice. The trypsin was inactivated with an equivalent volume of CP2 before centrifugation at 7500 × *g* for 7 min at 4°C. For our purposes (to maximize heart mitochondrial yield) the resultant pellet was resuspended in CP2, clarified with a 3000 × *g* spin before being resuspended in KME and combined with the SSM mitochondria. Organellar and mitochondrial fractions were quantitated using a BCA assay. Mitochondria were resuspended to 10 mg/ml in IB_C (cells) or KME (tissues) and if not

used immediately, aliquoted, snap frozen with liquid N_2 and stored at –80°C for downstream analyses.

Epitope mapping

A peptide scan consisting of 15mer peptides with an 11 amino acid overlap between adjacent peptides that spans the entire 262 amino acid TAZ protein was generated by JPT Peptide Technologies. The membrane was moistened with methanol prior to immunoblotting and the membrane subsequently regenerated with 100 mM β-mercaptoethanol, 1% (w/v) SDS, 62.5 mM Tris–HCl, pH 6.7, two more times to map epitopes bound by the different TAZ mAbs. The epitopes recognized by each of the three mAbs were determined by densitometry analysis of the immunoreactive PepSpots.

Immunoprecipitation

The TAZ mAb, 3D7F11, or normal mouse serum was conjugated to protein G-sepharose using the Seize X Protein A Immunoprecipitation kit and protocol (Pierce). Confluent T75 cm^2 flasks of the indicated cells were lysed with 1 ml RIPA lysis buffer and protein extracts quantified as described above. 1.5 mg cellular extract per cell line was diluted to 1 ml with protease inhibitor-spiked lysis buffer and rotated with 90 µl normal mouse serum-conjugated beads for 1 h at 4°C. After centrifugation at 376 × *g* for 5 min at 4°C, the pre-cleared lysates were transferred to tubes containing 90 µl 3D7F11-conjugated beads and rotated at 4°C for 4 h. Following low-speed centrifugation as before, unbound extract was collected for analysis and the bound material (both the preclear and IP beads) was sequentially washed (10 min rotating per wash) twice with Wash Buffer [0.1% (v/v) Triton X-100, 20 mM HEPES–KOH, pH 7.4, 50 mM NaCl, 1 mM EDTA, 2.5 mM $MgCl_2$, 0.1% (w/v) SDS; 1 ml per wash], twice with High Salt Wash Buffer [0.1% (v/v) Triton X-100, 20 mM HEPES–KOH, pH 7.4, 500 mM NaCl, 1 mM EDTA, 2.5 mM $MgCl_2$, 0.05% (w/v) deoxycholate; 1 ml per wash] and once with Low Salt Wash Buffer [0.1% (v/v) Triton X-100, 20 mM HEPES–KOH, pH 7.4, 1 mM EDTA, 2.5 mM $MgCl_2$, 0.05% (w/v) deoxycholate; 1 ml per wash]. To elute bound material, three sequential elutions were performed using 0.1 M glycine, pH 2.8, and the pooled eluates were neutralized with 50 µl 1 M Tris–Cl, pH 8.0. Eluates were transferred to a spin column (Pierce 1824826) and centrifuged for 2 min at 376 × *g* to reduce resin carry-over. Finally, the unbound extracts (preclear and IP beads) and eluates were TCA-precipitated [20% (v/v) TCA with 0.07% (v/v) deoxycholate] for 1 h on ice, the pellet fractions resuspended in a 1:1 mix of 2× reducing sample buffer and 0.1 M NaOH, and boiled for 5 min.

Genotyping taz^{TALEN} cells

Genomic DNA was extracted using the Gentra Puregene Cell Kit (Qiagen) and the genomic region surrounding the target site (exon1 extending into exon2, encompassing the ATG) was PCR amplified, digested with *Xba*I/*Hin*dIII (NEB), and ligated into pBSK(–). Transformants were analyzed by Sanger sequencing. As 293 cells are hypotriploid, sequences of at least 10 individual clones for each of the two taz^{TALEN} cell lines were obtained, revealing disruption of TAZ downstream of the initiation codon.

Quantitative RT-PCR

Total RNA was isolated from WT, taz^{TALEN} and taz^{TALEN} overexpressing *TAZ* alleles using the PureLink RNA Mini Kit with DNase treatment (Invitrogen). Twenty-five nanograms of RNA were analyzed in 20 µl reactions using the EXPRESS One-Step SYBR GreenER qRT-PCR Kit (Life Technologies) with 7500 Real-Time PCR Systems (Applied Biosystems) according to the manufacturer's instructions. Each reaction, including non-template controls, was performed at least in duplicate with a minimum of three different biological replicates and contained 50 nM ROX and 200 nM each of forward and reverse gene-specific primers designed with Primer3 (52). The reaction conditions were as follows: 5 min at 50°C, 2 min at 95°C, followed by 40 two-temperature cycles (15 s at 95°C and 1 min at 60°C) and melt curve profiling. Expression of *TAZ* was analyzed by the comparative C_T ($\Delta\Delta C_T$) method ($X_{Test}/X_{GAPDH} = 2^{-\Delta\Delta C_T}$) with *GAPDH* as an endogenous reference gene. Values were represented as mean $\Delta\Delta C_T \pm$ SEM or fold change ($2^{\Delta\Delta C_T}$) ± SD relative to *TAZ* expression in 293 Flp-In cells (Prism 6).

Import

Radiolabeled precursors were produced using an SP6 Quick Coupled Transcription/Translation system (Promega) spiked with Easy-Tag L-^{35}S-methionine (PerkinElmer). Radiolabeled precursors were incubated in import buffer (20 mM HEPES–KOH, pH 7.4, 250 mM sucrose, 80 mM KOAc, 5 mM MgOAc, 10 mM succinate and 5 mM methionine) with freshly isolated mitochondria for the indicated amount of time at 37 or 4°C, as specified. To dissipate the mitochondrial proton-motive force, mitochondria were pre-incubated with 1 µM valinomycin and 5 µM carbonyl cyanide *m*-chlorophenyl hydrazine for 5 min at 37°C. Import was stopped with an equal volume of ice-cold import buffer containing 20 µg/ml trypsin. Where indicated, the OMM was ruptured as already described in the presence of 20 µg/ml trypsin. Following 30 min on ice, 100 µg/ml soybean trypsin inhibitor was added and mitochondria were re-isolated by centrifugation at 21 000 × *g* for 5 min at 4°C. One hundred percent of each time point and 5% of imported precursors were resolved on 12% SDS–PAGE gels and analyzed by phosphoimaging.

Lipidomics

A defined amount of internal standards (0.1 nmol of $CL(14:0)_4$, 0.2 nmol of $BMP(14:0)_2$, 2.0 nmol of $PC(14:0)_2$, 0.1 nmol of $PG(14:0)_2$, 5.0 nmol of $PS(14:0)_2$, 0.5 nmol of $PE(14:0)_2$, 1.0 nmol of $PA(14:0)_2$, 2.0 nmol of $SM(14:0)_2$, 0.02 nmol of LPG(14:0), 0.1 nmol of LPE(14:0), 0.5 nmol of LPC(14:0), 0.1 nmol of LPA(14:0) (Avanti Polar Lipids) dissolved in 120 µl of chloroform/methanol (1:1, v/v)) and 1.5 ml of chloroform/methanol (1:1, v/v) were added to 1 mg mitochondria. Subsequently, the mixture was sonicated in a water bath for 5 min, followed by centrifugation at 15 000 × *g* for 5 min. The organic layer was transferred to a glass vial and dried under a nitrogen steam at 60°C. Subsequently, the residue was dissolved in 200 µl of chloroform/methanol/water (50:45:5, v/v/v) containing 0.01% of NH_4OH, and 10 µl of the solution was injected into the liquid chromatography-mass spectrometry (LC–MS) system. LC/MS analysis was performed as described in (36). In negative mode, mass spectra of phospholipid molecular species were obtained by continuous scanning from *m*/z 380 to 1500 with a scan time of 2 s. In positive mode, mass spectra of PC, LPC and SM were obtained by continuous scanning for product ions with *m*/z 184 from *m*/z 400 to 1000. Mass spectra for PE, LPE and PE plasmalogens were obtained by scanning on neutral losses of 141 from *m*/z 400 to 1000. The raw LC–MS data were converted to mzXML format using msConvert (53) for the negative scan data and ReAdW for the positive specific scan data. Details on the metabolic data preprocessing pipeline will be described elsewhere. Briefly, the dataset was processed using a semi-automated xcms-based metabolomics workflow (54) written in the R language and statistical environment

(http://www.r-project.org/). The workflow comprises pre-processing (peak-finding and quantification), identification of metabolites, isotope correction, normalization/scaling based on internal added standards and statistical analysis of the results.

Membrane association assays

Sonication experiments utilized 0.2 mg mitochondria and were performed in the absence of KCl as described (41). The supernatant and membrane fractions were separated by ultracentrifugation at 175 000 × *g* using a TLA120.1 rotor for 30 min at 4°C. Carbonate extraction was performed as described (30) except that 0.5 ml of 0.1 M Na_2CO_3 at the indicated pH was added to 0.1 mg mitochondria, and following 30 min on ice, the pellet and supernatant fractions were separated by centrifugation at 175 000 × *g* for 15 min at 4°C using a TLA120.1 rotor.

Blue native gel electrophoresis

Mitochondria were solubilized for 30 min on ice in 20 mM HEPES–KOH, 10% glycerol, 50 mM NaCl, 1 mM EDTA, 2.5 mM $MgCl_2$, pH 7.4 supplemented with 1% (w/v) (mouse tissues) or 1.25% (w/v) (human cells) digitonin (Biosynth International, Inc.) and protease inhibitors. Extracts were clarified by centrifugation for 30 min at 21 000 × *g* at 4°C and analyzed by 2D BN/SDS–PAGE exactly as described (46).

Digitonin fractionation assay

Digitonin-based submitochondrial localization was adapted from (41). In brief, 0.1 mg mitochondria were resuspended in 50 µl SEHK buffer (250 mM sucrose, 5 mM EDTA, pH 7.0, 10 mM HEPES–KOH, pH 7.4, 200 mM KCl) supplemented with 0–0.5% digitonin and 1 mM PMSF. Following a brief vortex on level 1, samples were incubated for 2 min on ice and solubilization stopped by adding 450 µl cold SEHK buffer. Solubilized proteins were separated from the membrane pellets by centrifugation at 100 000 × *g* for 10 min at 4°C. After the supernatant was TCA-precipitated, the membrane- and supernatant-derived pellets were resuspended in equal volumes of reducing sample buffer.

Protease-based assays

Freshly isolated mammalian mitochondria (0.2 mg) from cells or tissues were resuspended in iso-osmotic IB_c or KME buffers, respectively. To rupture the OMM, mitochondria (0.2 mg) were resuspended in 5 mM Tris–Cl, pH 7.5 for 30 min on ice; 0.5% (v/v) deoxycholate was added to further solubilize the IMM. Each of these conditions was performed in the absence and presence of 125 µg/ml pronase E. Pronase was inhibited with 5 mM PMSF and samples precipitated with 20% (v/v) TCA and 0.07% (v/v) deoxycholate, incubated at 60°C for 5 min followed by an hour on ice. Samples were centrifuged at 21 000 × *g* for 10 min at 4°C, washed with 1 ml of cold acetone, resuspended in a 1:1 mix of 2× reducing sample buffer:0.1 M NaOH and boiled for 5 min. To determine sensitivity to assorted proteases following heat denaturation, mitochondria (0.2 mg) were resuspended in 5 mM Tris–Cl, pH 7.5 containing 0.1% (v/v) SDS, kept on ice or incubated at 95°C for 5 min, and then 5 mM Tris–Cl, pH 7.5 with 0.1% SDS containing 250 µg/ml pronase E, 200 µg/ml proteinase K, or 40 µg/ml trypsin added. Following a 30 min incubation on ice, pronase E and proteinase K were inhibited with 5 mM PMSF and trypsin with 100 µg/ml soybean trypsin inhibitor. Every sample was precipitated with 20% (v/v) TCA and 0.07% (v/v) deoxycholate, incubated at 60°C for 5 min followed by an hour on ice. Samples were centrifuged at 21 000 × *g* for 10 min at 4°C, washed with 1 ml of cold acetone, resuspended in a 1:1 mix of 2× reducing sample buffer:0.1 M NaOH and boiled for 5 min.

Protein aggregation assay

Protein aggregation was determined in mitochondria (0.2 mg) isolated from 293 Flp-In cells exactly as previously described (31).

Phospholipid labeling and analyses

Cells were seeded onto 60 mm dishes or 6-well plates and allowed to grow to 50–70% confluency at 37°C, 5% CO_2. Following aspiration, regular media spiked with 2.5 µCi/ml $^{32}P_i$ was added and the cells incubated at 37°C, 5% CO_2 for 24 h. Cells were washed twice with ice-cold 1× PBS, detached in 0.8 ml IB_c buffer using a cell scraper, transferred to a microfuge tube, collected at 600 × *g* 5 min at 4°C, and resuspended in 0.1 ml IB_c buffer. Phospholipids were extracted from equal amounts of labeled cells, determined by liquid scintillation, as described (30) except that 0.9% (w/v) NaCl was used to initiate phase separation instead of ddH_2O. Samples were resuspended in chloroform, loaded onto ADAMANT TLC plates (Machery-Nagel), resolved once in chloroform:ethanol:H_2O:trimethylamine (30:35:7:35, v/v/v/v), and phospholipids visualized using a K-screen and FX-Imager (Bio-Rad Laboratories).

Electron microscopy

Cells were seeded onto 100 mm dishes and allowed to grow to ~70% confluence before fixing with 3.0% formaldehyde and 1.5% glutaraldehyde in 0.1 M sodium cacodylate, 5 mM $CaCl_2$, 2.5% (w/v) sucrose, pH 7.4, for 1 h at RT. Cells were washed three times for 15 min each with 0.1 M sodium cacodylate, 2.5% (w/v) sucrose, pH 7.4, and another three times for 5 min each with 50 mM Tris–HCl, 7.5% (w/v) sucrose, pH 7.4, prior to labeling with 0.5 mg/ml DAB and 0.015% H_2O_2 in 50 mM Tris–HCl, 7.5% (w/v) sucrose, pH 7.4 for 20–60 min. The labeling reaction was stopped by rinsing cells twice with 50 mM Tris–HCl, 7.5% (w/v) sucrose, pH 7.4, and once with 0.1 M sodium cacodylate, pH 7.4, 5 mM $CaCl_2$, 2.5% (w/v) sucrose, before harvesting the cells with 1 ml of 0.1 mM cacodylate buffer, pH 7.4; and pelleting the cells in 1.5 ml Eppendorf tube. Cells were pelleted progressively by spinning from 3000 to 12 000 rpm over the course of 10 min and the pellet was post-fixed in reduced osmium tetroxide (1% OsO_4, 1% potassium ferrocyanide in 0.1 M sodium cacodylate, 5 mM $CaCl_2$, pH 7.4) for 45 min at RT. The pellets were washed thoroughly with 0.1 M sodium cacodylate, pH 7.4, 5 mM $CaCl_2$, 2.5% (w/v) sucrose several times until solution becomes clear, dehydrated through a graded series of ice-cold ethanol, and subsequently embedded in Epon resin. Sections were cut on a Leica UCT ultramicrotome and observed on an FEI Tecnai 12 transmission electron microscope at 100 kV. Images were captured with a Soft Imaging System Megaview III digital camera and figures were assembled in Adobe Photoshop and Illustrator with only linear adjustments in contrast and brightness.

Cycloheximide chase

Cell culture medium lacking antibiotics but containing 100 µg/ml cycloheximide was added to confluent 6-well plates and incubated at 37°C, 5% CO_2. At the designated times, cells were solubilized with 100 µl 1% (w/v) SDS and diluted to 0.5% SDS, 1% β-mercaptoethanol with 2% (v/v) β-mercaptoethanol. After denaturing the lysates at 100°C for 10 min, protein was quantified using the Bradford method (Bio-Rad).

Transacylation assay

The transacylase assays were performed as previously described (16,32) using 1 nmol of 1-[^{14}C]palmitoyl-2-lyso-PC (0.05 mCi; PerkinElmerLife Sciences) per reaction in 0.2 ml reaction buffer (10 mM β-mercaptoethanol, 0.5 mM EDTA, 50 mM Tris, pH 7.4). To initiate the reactions, ∼125 μg mitochondria (the exact amount was determined by the BCA assay) were added, the reactions vortexed on high for 1 s, and incubated with shaking at 220 rpm for 5 min at 37°C. Lipid extraction, thin layer chromatography separation, image acquisition and analyses were executed as described (32).

Data analysis

Band densitometry analyses were performed using Quantity One (Bio-Rad) or ImageJ (55). With the exception of the data in Figures 2D and 7D, statistical analyses were performed using SigmaPlot 11 software (Systat Software) and all comparisons performed by *t*-test or one-way analysis of variance with Holm-Sidak pairwise comparisons. For Figures 2D and 7D, comparisons were performed using one-way analysis of variance with Geisser-Greenhouse correction Tukey's multiple comparison test available in the Prism 6 software (GraphPad). All graphs report the mean ± SEM.

Supplementary Material

Supplementary Material is available at *HMG* online.

Acknowledgements

We are grateful to Kim-Vy Nguyen (Andrew Ewald lab) for providing all the mouse tissues used for experiments in this paper.

Conflict of Interest statement. None declared.

Funding

This work was supported by the Barth Syndrome Foundation (to S.M.C.); the National Institutes of Health (R00HL089185 and R01HL108882 to S.M.C., R01GM061721 to C.M.K., NIH/ORIP 1S10RR023454-01 to J.M.M.); and a pre-doctoral fellowship from the American Heart Association (12PRE11910004 to Y.-W.L.).

References

1. Claypool, S.M. and Koehler, C.M. (2012) The complexity of cardiolipin in health and disease. *Trends Biochem. Sci.*, **37**, 32–41.
2. Zhang, J., Guan, Z., Murphy, A.N., Wiley, S.E., Perkins, G.A., Worby, C.A., Engel, J.L., Heacock, P., Nguyen, O.K., Wang, J.H. *et al.* (2011) Mitochondrial phosphatase PTPMT1 is essential for cardiolipin biosynthesis. *Cell Metab.*, **13**, 690–700.
3. Claypool, S.M. (2009) Cardiolipin, a critical determinant of mitochondrial carrier protein assembly and function. *Biochim. Biophys. Acta*, **1788**, 2059–2068.
4. Gebert, N., Joshi, A.S., Kutik, S., Becker, T., McKenzie, M., Guan, X.L., Mooga, V.P., Stroud, D.A., Kulkarni, G., Wenk, M. R. *et al.* (2009) Mitochondrial cardiolipin involved in outer-membrane protein biogenesis: implications for Barth syndrome. *Curr. Biol.*, **19**, 2133–2139.
5. Kutik, S., Rissler, M., Guan, X.L., Guiard, B., Shui, G., Gebert, N., Heacock, P.N., Rehling, P., Dowhan, W., Wenk, M.R. *et al.* (2008) The translocator maintenance protein Tam41 is required for mitochondrial cardiolipin biosynthesis. *J. Cell Biol.*, **183**, 1213–1221.
6. Lange, C., Nett, J.H., Trumpower, B.L. and Hunte, C. (2001) Specific roles of protein-phospholipid interactions in the yeast cytochrome bc1 complex structure. *EMBO J.*, **20**, 6591–6600.
7. Acín-Pérez, R., Fernández-Silva, P., Peleato, M.L., Pérez-Martos, A. and Enriquez, J.A. (2008) Respiratory Active Mitochondrial Supercomplexes. *Mol. Cell*, **32**, 529–539.
8. Pfeiffer, K., Gohil, V., Stuart, R.A., Hunte, C., Brandt, U., Greenberg, M.L. and Schagger, H. (2003) Cardiolipin stabilizes respiratory chain supercomplexes. *J. Biol. Chem.*, **278**, 52873–52880.
9. Zhang, M., Mileykovskaya, E. and Dowhan, W. (2002) Gluing the respiratory chain together. Cardiolipin is required for supercomplex formation in the inner mitochondrial membrane. *J. Biol. Chem.*, **277**, 43553–43556.
10. DeVay, R.M., Dominguez-Ramirez, L., Lackner, L.L., Hoppins, S., Stahlberg, H. and Nunnari, J. (2009) Coassembly of Mgm1 isoforms requires cardiolipin and mediates mitochondrial inner membrane fusion. *J. Cell Biol.*, **186**, 793–803.
11. Montessuit, S., Somasekharan, S.P., Terrones, O., Lucken-Ardjomande, S., Herzig, S., Schwarzenbacher, R., Manstein, D.J., Bossy-Wetzel, E., Basanez, G., Meda, P. *et al.* (2010) Membrane remodeling induced by the dynamin-related protein Drp1 stimulates Bax oligomerization. *Cell*, **142**, 889–901.
12. Chu, C.T., Ji, J., Dagda, R.K., Jiang, J.F., Tyurina, Y.Y., Kapralov, A.A., Tyurin, V.A., Yanamala, N., Shrivastava, I.H., Mohammadyani, D. *et al.* (2013) Cardiolipin externalization to the outer mitochondrial membrane acts as an elimination signal for mitophagy in neuronal cells. *Nat. Cell Biol.*, **15**, 1197–1205.
13. Gonzalvez, F., Schug, Z.T., Houtkooper, R.H., MacKenzie, E.D., Brooks, D.G., Wanders, R.J., Petit, P.X., Vaz, F.M. and Gottlieb, E. (2008) Cardiolipin provides an essential activating platform for caspase-8 on mitochondria. *J. Cell Biol.*, **183**, 681–696.
14. Baile, M.G., Lu, Y.W. and Claypool, S.M. (2014) The topology and regulation of cardiolipin biosynthesis and remodeling in yeast. *Chem. Phys. Lipids*, **179**, 25–31.
15. Schlame, M., Ren, M., Xu, Y., Greenberg, M.L. and Haller, I. (2005) Molecular symmetry in mitochondrial cardiolipins. *Chem. Phys. Lipids*, **138**, 38–49.
16. Xu, Y., Malhotra, A., Ren, M. and Schlame, M. (2006) The enzymatic function of tafazzin. *J. Biol. Chem.*, **281**, 39217–39224.
17. Barth, P.G., Scholte, H.R., Berden, J.A., Van der Klei-Van Moorsel, J.M., Luyt-Houwen, I.E., Van 't Veer-Korthof, E.T., Van der Harten, J.J. and Sobotka-Plojhar, M.A. (1983) An X-linked mitochondrial disease affecting cardiac muscle, skeletal muscle and neutrophil leucocytes. *J. Neurol. Sci.*, **62**, 327–355.
18. Bione, S., D'Adamo, P., Maestrini, E., Gedeon, A.K., Bolhuis, P. A. and Toniolo, D. (1996) A novel X-linked gene, G4.5. is responsible for Barth syndrome. *Nat. Genet.*, **12**, 385–389.
19. Valianpour, F., Mitsakos, V., Schlemmer, D., Towbin, J.A., Taylor, J.M., Ekert, P.G., Thorburn, D.R., Munnich, A., Wanders, R. J., Barth, P.G. *et al.* (2005) Monolysocardiolipins accumulate in Barth syndrome but do not lead to enhanced apoptosis. *J. Lipid Res.*, **46**, 1182–1195.
20. Houtkooper, R.H., Turkenburg, M., Poll-The, B.T., Karall, D., Perez-Cerda, C., Morrone, A., Malvagia, S., Wanders, R.J., Kulik, W. and Vaz, F.M. (2009) The enigmatic role of tafazzin in cardiolipin metabolism. *Biochim. Biophys. Acta*, **1788**, 2003–2014.
21. Dudek, J., Cheng, I.F., Balleininger, M., Vaz, F.M., Streckfuss-Bomeke, K., Hubscher, D., Vukotic, M., Wanders, R.J., Rehling, P. and Guan, K. (2013) Cardiolipin deficiency affects respiratory chain function and organization in an induced pluripotent stem cell model of Barth syndrome. *Stem Cell Res.*, **11**, 806–819.

22. Gonzalvez, F., D'Aurelio, M., Boutant, M., Moustapha, A., Puech, J.P., Landes, T., Arnaune-Pelloquin, L., Vial, G., Taleux, N., Slomianny, C. *et al.* (2013) Barth syndrome: cellular compensation of mitochondrial dysfunction and apoptosis inhibition due to changes in cardiolipin remodeling linked to tafazzin (TAZ) gene mutation. *Biochim. Biophys. Acta*, **1832**, 1194–1206.
23. McKenzie, M., Lazarou, M., Thorburn, D.R. and Ryan, M.T. (2006) Mitochondrial respiratory chain supercomplexes are destabilized in Barth Syndrome patients. *J. Mol. Biol.*, **361**, 462–469.
24. Wang, G., McCain, M.L., Yang, L., He, A., Pasqualini, F.S., Agarwal, A., Yuan, H., Jiang, D., Zhang, D., Zangi, L. *et al.* (2014) Modeling the mitochondrial cardiomyopathy of Barth syndrome with induced pluripotent stem cell and heart-on-chip technologies. *Nat. Med.*, **20**, 616–623.
25. Lu, Y.W. and Claypool, S.M. (2015) Disorders of phospholipid metabolism: an emerging class of mitochondrial disease due to defects in nuclear genes. *Front Genet.*, **6**, 3.
26. Davey, K.M., Parboosingh, J.S., McLeod, D.R., Chan, A., Casey, R., Ferreira, P., Snyder, F.F., Bridge, P.J. and Bernier, F.P. (2006) Mutation of DNAJC19, a human homologue of yeast inner mitochondrial membrane co-chaperones, causes DCMA syndrome, a novel autosomal recessive Barth syndrome-like condition. *J. Med. Genet.*, **43**, 385–393.
27. Mayr, J.A., Haack, T.B., Graf, E., Zimmermann, F.A., Wieland, T., Haberberger, B., Superti-Furga, A., Kirschner, J., Steinmann, B., Baumgartner, M.R. *et al.* (2012) Lack of the mitochondrial protein acylglycerol kinase causes Sengers syndrome. *Am. J. Hum. Genet.*, **90**, 314–320.
28. Richter-Dennerlein, R., Korwitz, A., Haag, M., Tatsuta, T., Dargazanli, S., Baker, M., Decker, T., Lamkemeyer, T., Rugarli, E.I. and Langer, T. (2014) DNAJC19, a mitochondrial cochaperone associated with cardiomyopathy, forms a complex with prohibitins to regulate cardiolipin remodeling. *Cell Metab.*, **20**, 158–171.
29. Wortmann, S.B., Vaz, F.M., Gardeitchik, T., Vissers, L.E., Renkema, G.H., Schuurs-Hoeijmakers, J.H., Kulik, W., Lammens, M., Christin, C., Kluijtmans, L.A. *et al.* (2012) Mutations in the phospholipid remodeling gene SERAC1 impair mitochondrial function and intracellular cholesterol trafficking and cause dystonia and deafness. *Nat. Genet.*, **44**, 797–802.
30. Claypool, S.M., McCaffery, J.M. and Koehler, C.M. (2006) Mitochondrial mislocalization and altered assembly of a cluster of Barth syndrome mutant tafazzins. *J. Cell Biol.*, **174**, 379–390.
31. Claypool, S.M., Whited, K., Srijumnong, S., Han, X. and Koehler, C.M. (2011) Barth syndrome mutations that cause tafazzin complex lability. *J. Cell Biol.*, **192**, 447–462.
32. Whited, K., Baile, M.G., Currier, P. and Claypool, S.M. (2013) Seven functional classes of Barth syndrome mutation. *Hum. Mol. Genet.*, **22**, 483–492.
33. Gonzalez, I.L. (2005) Barth syndrome: TAZ gene mutations, mRNAs, and evolution. *Am. J. Med. Genet. A*, **134**, 409–414.
34. Vaz, F.M., Houtkooper, R.H., Valianpour, F., Barth, P.G. and Wanders, R.J. (2003) Only one splice variant of the human TAZ gene encodes a functional protein with a role in cardiolipin metabolism. *J. Biol. Chem.*, **278**, 43089–43094.
35. Diehl, J.A., Zindy, F. and Sherr, C.J. (1997) Inhibition of cyclin D1 phosphorylation on threonine-286 prevents its rapid degradation via the ubiquitin-proteasome pathway. *Genes Dev.*, **11**, 957–972.
36. Houtkooper, R.H., Rodenburg, R.J., Thiels, C., van Lenthe, H., Stet, F., Poll-The, B.T., Stone, J.E., Steward, C.G., Wanders, R. J., Smeitink, J. *et al.* (2009) Cardiolipin and monolysocardiolipin analysis in fibroblasts, lymphocytes, and tissues using high-performance liquid chromatography-mass spectrometry as a diagnostic test for Barth syndrome. *Anal. Biochem.*, **387**, 230–237.
37. Claypool, S.M., Boontheung, P., McCaffery, J.M., Loo, J.A. and Koehler, C.M. (2008) The cardiolipin transacylase, tafazzin, associates with two distinct respiratory components providing insight into Barth syndrome. *Mol. Biol. Cell*, **19**, 5143–5155.
38. Brandner, K., Mick, D.U., Frazier, A.E., Taylor, R.D., Meisinger, C. and Rehling, P. (2005) Taz1, an outer mitochondrial membrane protein, affects stability and assembly of inner membrane protein complexes: implications for Barth Syndrome. *Mol. Biol. Cell*, **16**, 5202–5214.
39. Hung, V., Zou, P., Rhee, H.W., Udeshi, N.D., Cracan, V., Svinkina, T., Carr, S.A., Mootha, V.K. and Ting, A.Y. (2014) Proteomic mapping of the human mitochondrial intermembrane space in live cells via ratiometric APEX tagging. *Mol. Cell*, **55**, 332–341.
40. Lam, S.S., Martell, J.D., Kamer, K.J., Deerinck, T.J., Ellisman, M. H., Mootha, V.K. and Ting, A.Y. (2015) Directed evolution of APEX2 for electron microscopy and proximity labeling. *Nat. Methods*, **12**, 51–54.
41. Baile, M.G., Whited, K. and Claypool, S.M. (2013) Deacylation on the matrix side of the mitochondrial inner membrane regulates cardiolipin remodeling. *Mol. Biol. Cell*, **24**, 2008–2020.
42. Baile, M.G., Sathappa, M., Lu, Y.W., Pryce, E., Whited, K., McCaffery, J.M., Han, X., Alder, N.N. and Claypool, S.M. (2014) Unremodeled and remodeled cardiolipin are functionally indistinguishable in yeast. *J. Biol. Chem.*, **289**, 1768–1778.
43. Schlame, M., Acehan, D., Berno, B., Xu, Y., Valvo, S., Ren, M., Stokes, D.L. and Epand, R.M. (2012) The physical state of lipid substrates provides transacylation specificity for tafazzin. *Nat. Chem. Biol.*, **8**, 862–869.
44. Merkwirth, C., Dargazanli, S., Tatsuta, T., Geimer, S., Lower, B., Wunderlich, F.T., von Kleist-Retzow, J.C., Waisman, A., Westermann, B. and Langer, T. (2008) Prohibitins control cell proliferation and apoptosis by regulating OPA1-dependent cristae morphogenesis in mitochondria. *Genes Dev.*, **22**, 476–488.
45. Ho, S.N., Hunt, H.D., Horton, R.M., Pullen, J.K. and Pease, L.R. (1989) Site-directed mutagenesis by overlap extension using the polymerase chain reaction. *Gene*, **77**, 51–59.
46. Claypool, S.M., Oktay, Y., Boontheung, P., Loo, J.A. and Koehler, C.M. (2008) Cardiolipin defines the interactome of the major ADP/ATP carrier protein of the mitochondrial inner membrane. *J. Cell Biol.*, **182**, 937–950.
47. Panneels, V., Schussler, U., Costagliola, S. and Sinning, I. (2003) Choline head groups stabilize the matrix loop regions of the ATP/ADP carrier ScAAC2. *Biochem. Biophys. Res. Commun.*, **300**, 65–74.
48. Claypool, S.M., Dickinson, B.L., Yoshida, M., Lencer, W.I. and Blumberg, R.S. (2002) Functional reconstitution of human FcRn in Madin-Darby canine kidney cells requires co-expressed human beta 2-microglobulin. *J. Biol. Chem.*, **277**, 28038–28050.
49. Frezza, C., Cipolat, S. and Scorrano, L. (2007) Organelle isolation: functional mitochondria from mouse liver, muscle and cultured fibroblasts. *Nat. Protoc.*, **2**, 287–295.
50. O'Shea, K.M., Khairallah, R.J., Sparagna, G.C., Xu, W., Hecker, P. A., Robillard-Frayne, I., Des Rosiers, C., Kristian, T., Murphy, R.C., Fiskum, G. *et al.* (2009) Dietary omega-3 fatty acids alter cardiac mitochondrial phospholipid composition and delay Ca2+-induced permeability transition. *J. Mol. Cell. Cardiol.*, **47**, 819–827.
51. Palmer, J.W., Tandler, B. and Hoppel, C.L. (1977) Biochemical properties of subsarcolemmal and interfibrillar mitochondria isolated from rat cardiac muscle. *J. Biol. Chem.*, **252**, 8731–8739.

52. Untergasser, A., Nijveen, H., Rao, X., Bisseling, T., Geurts, R. and Leunissen, J.A. (2007) Primer3Plus, an enhanced web interface to Primer3. *Nucleic Acids Res.*, **35**, W71–W74.
53. Chambers, M.C., Maclean, B., Burke, R., Amodei, D., Ruderman, D.L., Neumann, S., Gatto, L., Fischer, B., Pratt, B., Egertson, J. *et al.* (2012) A cross-platform toolkit for mass spectrometry and proteomics. *Nat. Biotech.*, **30**, 918–920.
54. Smith, C.A., Want, E.J., O'Maille, G., Abagyan, R. and Siuzdak, G. (2006) XCMS: processing mass spectrometry data for metabolite profiling using nonlinear peak alignment, matching, and identification. *Anal. Chem.*, **78**, 779–787.
55. Schneider, C.A., Rasband, W.S. and Eliceiri, K.W. (2012) NIH Image to ImageJ: 25 years of image analysis. *Nat. Methods*, **9**, 671–675.